Dynamic Modulation of Matrix Adhesiveness Induces Epithelial-to-Mesenchymal Transition in Prostate Cancer Cells in 3D

Mugdha Pol,^{1\$} Hanyuan Gao,^{2\$} He Zhang,² Olivia J. George,² Joseph M. Fox,^{2,3} Xinqiao Jia^{1,2,4,5*}

¹Department of Biological Sciences, University of Delaware, Newark, Delaware, USA.

²Department of Materials Science and Engineering, University of Delaware, Newark, Delaware, USA.

³Department of Chemistry and Biochemistry, University of Delaware, Newark, Delaware, USA.

⁴Department of Biomedical Engineering, University of Delaware, Newark, Delaware, USA.

⁵Delaware Biotechnology Institute, University of Delaware, Newark, Delaware, USA.

\$These authors contributed equally to this work.

*Corresponding author:

Dr. Xinqiao Jia, 201 DuPont Hall, Department of Materials Science and Engineering, University of Delaware, Newark, DE, 19716, USA. Phone: 302-831-6553, Fax: 302-831-4545, E-mail: xjia@udel.edu.

Keywords: Prostate Cancer, Hydrogels, RGD, Epithelial-to-Mesenchymal Transition, Invadopodia.

ABSTRACT

Synthetic matrices with dynamic presentation of cell guidance cues are needed for the development of physiologically relevant in vitro tumor models. Towards the goal of mimicking prostate cancer progression and metastasis, we engineered a tunable hyaluronic acid-based hydrogel platform with protease degradable and cell adhesive properties employing bioorthogonal tetrazine ligation with strained alkenes. The synthetic matrix was first fabricated via a slow tetrazine-norbornene reaction, then temporally modified via a diffusion-controlled method using trans-cyclooctene, a fierce dienophile that reacts with tetrazine with an unusually fast rate. The encapsulated DU145 prostate cancer single cells spontaneously formed multicellular tumoroids after 7 days of culture. In situ modification of the synthetic matrix via covalent tagging of cell adhesive RGD peptide induced tumoroid decompaction and the development of cellular protrusions. RGD tagging did not compromise the overall cell viability, nor did it induce cell apoptosis. In response to increased matrix adhesiveness, DU145 cells dynamically loosen cellcell adhesion and strengthen cell-matrix interactions to promote an invasive phenotype. Characterization of the 3D cultures by immunocytochemistry and gene expression analyses demonstrated that cells invaded into the matrix via a mesenchymal like migration, with upregulation of major mesenchymal markers, and down regulation of epithelial markers. The tumoroids formed cortactin positive invadopodia like structures, indicating active matrix remodeling. Overall, the engineered tumor model can be utilized to identify potential molecular targets and test pharmacological inhibitors, thereby accelerating the design of innovative strategies for cancer therapeutics.

INTRODUCTION

In the United States, prostate cancer (PCa) is the most frequently diagnosed non-cutaneous malignancy in men. At the early stage of the disease, it is characterized by symptom free and undetected slow growth of tumor(1, 2), with a five-year survival rate close to 100%. Approximately 50% of PCa patients can develop metastasis, where PCa cells escape from the primary tumor to invade the nerves, spread to the lymph nodes, or grow in the bones. Once metastasized, the survival rate drops to 30%(3). Prostate cancer is typically diagnosed by transrectal ultrasound guided prostatic biopsies and the type of treatment is chosen based on different prognostic parameters, such as prostatic specific antigen levels in serum, Gleason score, and patient's age. Current treatment approaches include surgery, chemotherapy, radiation therapy, hormonal therapy, and cryosurgery(4, 5).

Deeper understanding of mechanisms underlying tumorigenesis will enable the development of better treatment options. Tumors are complex and heterogenous structures, and the dynamic reciprocity between cancer cells and the surrounding microenvironment is crucial for disease progression(6). The biochemical and biomechanical characteristics of the tumor niche control cell differentiation, dissemination, and invasion. Various extracellular matrix (ECM) components, such as fibronectin and collagen, associate with the plasma membrane of cancer cells via integrins, and through the formation of focal adhesion complexes, connect to the intracellular cytoskeleton to control cell morphology and mobility. These ECM signals are then relayed to the nucleus to regulate gene expression or release of specific ECM degrading proteases, such as matrix metalloproteases (MMP)(7, 8).

An important determinant of tumor behavior is its ability to breach the basement membrane and spread outside the confines of the organ of origin(9, 10). Cancer metastasis occurs through multiple mechanisms, one of which involves epithelial-to-mesenchymal transition (EMT). EMT occurs when epithelial cells weaken their cell-cell contacts, lose apical basal polarity, and reorganize the cytoskeleton to acquire a migratory mesenchymal phenotype. EMT occurs in

a small subset of tumor cells and can be confirmed by comprehensive analyses of cellular deformations and cytoskeletal protrusions for directed migration(11, 12). These transformed cells can detach from the original tumor mass and squeeze through the dense ECM or proteolytically digest the complex microenvironment. To navigate through the diverse environments, cancer cells must undergo cellular adaptations to remodel the ECM, overcome extracellular barriers, interact with neighboring cells or surrounding matrix through biochemical and/or biomechanical mechanisms(8, 13, 14). Depending on ECM composition, density and stiffness, the mode of cancer cell migration can vary among mesenchymal-like invasive migration, amoeboid blebbing, and single, chain or collective migration(15).

To dissect molecular mechanisms involved in metastasis, it is necessary to establish 3D biomimetic tumor models(16) by incorporating cancer cells in naturally derived or synthetic matrices. EMT and loss of polarity were first observed in lens epithelial cells embedded in a collagen gel; in response to ECM cues, these cells undergo extreme cytoskeletal reorganization, adopt elongated morphology, develop pseudopodia-like structures and become migratory(17). Mammary epithelial cancer cells embedded in Matrigel adopt a spindle like elongated morphology, capable of contracting and extending to the surrounding matrix(18, 19). When grown in Matrigel, prostate epithelial cells from cancerous tissues exhibited different morphologies. Most formed poorly differentiated spheroids, but the aggressive PC-3 and PC-3M cells formed intact spheroids and then spontaneously transformed into invasive cells with cellular protrusions. These cells might have previously undergone EMT, which was momentarily repressed, and with signals from ECM, transformed into invasive cellular structures. The less invasive prostate cancer cell line DU145 formed intact and polarized spheroids, without any sign of invasive protrusions in Matrigel(18-20).

Compared to reconstituted natural ECM gels, synthetic biomaterials offer consistency and reproducibility, with added advantages of tunability in materials properties and customization of the microenvironment based on the disease stage(8, 21, 22). The engineered matrices also

enable cell mediated remodeling of synthetic tumor microenvironment, thus more closely mimicking the *in vivo* situation. Hyaluronic acid (HA), a non-sulfated glycosaminoglycan, is a major component of tumor microenvironment. Through the interactions with HA-degrading enzymes, hyaluronidases (HAases), cell surface receptors, cluster of differentiation 44 (CD44) and receptor for hyaluronan-mediated motility (RHAMM), HA activates signaling pathways that direct cell adhesion, differentiation, and migration. Additionally, HA can be readily and reproducibly modified to install reactive handles and to incorporate ECM-derived signals(23, 24). Using HA-based hydrogels, we showed that less invasive LNCaP cells encapsulated as single cells spontaneously formed multicellular tumoroids. However, these tumoroids remained immobilized in the hydrogel, without any sign of dissemination or invasion into the surrounding matrix(24-26). On the other hand, when encapsulated in HA gels established via the dynamic covalent bonds (i.e., hydrazone linkages), the more aggressive C4-2 and C4-2B cells formed irregular cell aggregates with occasional invadopodia-like structures(24, 27).

With an overarching goal of modeling prostate cancer metastasis, we report a novel HA-based hydrogel platform that is physiologically relevant and dynamically tunable; it not only recreates the pathophysiological features of the primary tumor, but also recapitulates the dynamic alternation of ECM compositions during metastasis. The synthetic matrix is established employing bioorthogonal tetrazine ligation with slow (norbornene, Nb, $k_2 \sim 10^{-2}$ - 10^0 M⁻¹s⁻¹) and fast (*trans*-cyclooctene, TCO, $k_2 \sim 10^5$ - 10^6 M⁻¹s⁻¹) dienophiles(28-31). The slow tetrazine-Nb reaction was employed to create a permissive network for the clonal expansion of single PCa cells, while the ultrafast, and extremely efficient tetrazine-TCO reaction(28, 32, 33) was utilized to conjugate cell-adhesive peptides to the living construct in a time-delayed manner to induce cell dissemination and invasion. Using brain metastasized prostate cancer cells, we investigated how biochemical and biomechanical signals in the synthetic ECM promoted the formation of compact multicellular spheroids. We further interrogated how the alteration of ECM adhesiveness induced phenotypical changes, and stimulated spheroids decompaction and cell invasion into the surrounding matrix.

We systematically analyzed cellular growth, phenotype, dissemination, and invasion in the engineered environment. Overall, this engineered hydrogel platform is a tunable and experimentally tractable alternative to study underlying mechanisms of tumor progression and evaluate efficacy of pharmacological inhibitors.

EXPERIMENTAL SECTION

1. Materials and Reagents

Hyaluronic acid (HA, sodium salt, 430 kDa) was a generous gift from Sanofi/Genzyme Corporation (Cambridge, MA). Methyl tetrazine-NHS ester was purchased from Click Chemistry Tools (Scottsdale, AZ). All Fmoc-protected amino acids were purchased from AAPPTec Inc. (Louisville, KY). Rink amide MBHA resin was purchased from EMD Millipore Corporation (Billerica, MA). Ethyl cyanohydroxyiminoacetate (Oxyma) was purchased from CEM Corporation (Matthews, NC). Diisopropylcarbodiimide (DIC) was purchased from Chem-Impex International Inc. (Wood Dale, IL). Hydrazine monohydrate and triisopropylsilane (TIPS) were purchased from Acros Organics (Carlsbad, CA). 1-Ethyl-3-(-3-dimethylaminopropyl) carbodiimide hydrochloride (EDC) and piperidine were purchased from Sigma-Aldrich (St. Louis, MO). Diisopropylethylamine (DIPEA), triethylamine (TEA), collagenase (type II and IV), common organic solvents and cell culture reagents were purchased from ThermoFisher Scientific (Waltham, MA) unless otherwise specified.

2. Hydrogel Synthesis and Characterization

2.1. Synthesis of hydrogel building blocks

Tetrazine functionalized HA (HA-Tz), with ~22% Tz incorporation as confirmed by UV-vis (Fig. S1) and ¹H NMR (Fig. S2), was synthesized following our previously reported procedure(*32*, *34*). A protease degradable peptide, SMR (Ac-KGGVPM**S**↓**MR**GGGGK-NH₂), was synthesized following standard solid-phase peptide synthesis protocol using a Liberty Blue Peptide

Synthesizer (CEM Corporation, Matthews, NC). To synthesize norbornene-functionalized protease degradable crosslinker (SMR-bisNb), a round bottom flask was charged with SMR (0.108 mmol) in dimethylformamide (DMF, 1.2 mL). Next, 5-norbornene-2-carboxylic acid Nhydroxysuccinimide ester (Nb-NHS ester, 1.5 equiv. to amine) and TEA (1.25 equiv. to amine) were introduced. The reaction was allowed to proceed overnight under stirring at ambient temperature. The product was obtained by precipitation in ether, followed by centrifugation and repeated wash with ether. The crude product was purified using a preparative high-performance liquid chromatography (HPLC, Waters Corporation, Milford, MA) with a C18 column (Luna 5 µm, 100 Å, 250 × 21.2 mm, Phenomenex, Torrance, CA). Samples were run with a gradient of 10 to 60% acetonitrile in water over 25 min at a flow rate of 10 mL/min at 25 °C using a UV-vis detector at 214 nm, and then lyophilized to yield SMR-bisNb (0.059 mmol, 55%) as a fluffy white solid. The purity of the product was confirmed via an analytical HPLC (Shimadzu Scientific Instruments, Columbia, MD) as >95%, and the mass was characterized through a Xevo G2-S QTof mass spectrometry (Waters Corporation, Milford, MA) as 1599.62 Da (expected 1599.94 Da) (Fig. S3-S8). RGD (Ac-GKGYGRGDSPG-NH₂) and RGE (Ac-GKGYGRGESPG-NH₂) peptides prepared on the Liberty Blue synthesizer were treated with TCO nitrophenyl carbonate to produced RGD-TCO and RGE-TCO (Fig. S9-S20)(33, 35, 36).

2.2. Hydrogel synthesis and interfacial ligation

HA-Tz and SMR-bisNb were separately dissolved in PBS at 2 wt% and 10 mM, respectively. The stock solutions were combined along with phosphate buffered saline (PBS, pH 7.4) to yield a final Tz and Nb concentration of 5.0 mM and 2.5 mM, respectively. After mixing for 10 min, 300 μL of the viscous solution was transferred into a 12 mm PTFE cell culture insert (Millicell 0.4 μm, EMD Millipore Corporation, Billerica, MA) and incubated at 37°C for 1 h. to allow complete gelation. Next, 300 μL PBS solution containing a total of 4 mM TCO-conjugated peptides was loaded on the top of the hydrogel to introduce RGD or RGE signals to the network. The

diffusion controlled interfacial ligation was allowed to proceed for 10 h at 37°C before the TCO reservoir was removed. To assess spatial distribution of peptide in the modulated hydrogel, a TCO reservoir containing 10 µM Cy5-TCO and 4 mM RGD-TCO was used for interfacial ligation. Confocal microscopy was performed on the resultant gel using Zeiss LSM 880 with C-Apochromat 10x/0.45W objective. Images were captured with a 20.5-µm z-axis step size. 3D reconstruction of z-stack was conducted with x, y, and z dimensions of 600, 600, and 1400 µm respectively. To modulate RGD density in the HA gel, TCO reservoirs with RGD-TCO and RGE-TCO mixed at a molar ratio of 1:0, 1:1.5, and 0:1 was used to generate modified constructs as RGD-H, RGD-L and RGD-0, respectively.

2.3. Peptide conjugation efficiency

Upon completion of interfacial ligation, the TCO reservoir was removed, and the hydrogel construct was incubated in PBS under gentle shaking at 37°C. At 3, 6, 12, and 24 h, the wash buffer was collected, and fresh PBS was introduced. The collected wash buffer was subsequently lyophilized and the solid was reconstituted as concentrated solution in PBS for UV-vis (Agilent Technologies, Santa Clara, CA) analysis at 275 nm (tyrosine, Y). The conjugation efficiency was calculated according to the standard curves constructed using known amounts of RGD/E (Fig. S21).

2.4. Hydrogel degradation

Hydrogels prepared as described above in cell culture inserts were immersed in Hanks' Balanced Salt Solution (HBSS, ThermoFisher Scientific) at 37°C for 12 h and the wet weight of the hydrogel was recorded. Collagenase II or IV solution (100 U/mL in HBSS) was loaded in and outside the insert and the samples were incubated on a shaker at 37°C. The collagenase solution was refreshed every 12 h, and the wet gel mass was recorded. HBSS was used as a control and all measurements were conducted in triplicate.

2.4. Oscillatory rheology

A stress-controlled rheometer (AR-G2, TA Instruments, New Castle, DE) was used to characterize the rheological properties of synthetic hydrogels. Once combined, the hydrogel precursor solution (40 µL) was immediately loaded on the bottom plate. A 20-mm parallel plate geometry was lowered to maintain a gap size of 100 µm. A time sweep experiment was conducted for 8 h at a frequency of 1 Hz and a strain of 1%, followed by a frequency sweep measured from 0.1 to 10 Hz with a fixed strain of 1%. Separately, gels were made in cell culture inserts and interfacial ligation of RGD and RGE peptides were carried out as described above. After PBS wash, the disk was removed from the insert, loaded on the bottom plate, and tested using an 8-mm parallel plate geometry with an axial force of 0.03 N. A 20-min time sweep was conducted at a frequency of 1 Hz and a strain of 1%, followed by a frequency sweep measured from 0.1 to 10 Hz at a strain of 1%. Mineral oil was applied around the geometry to prevent sample drying during the measurements. All measurements were conducted in triplicate at 37°C.

3. Development and Characterization of Cellular Construct.

3.1. Cell maintenance

DU145 prostate cancer cells were purchased from American Type Culture Collection (ATCC, Manassas, VA). Cells were maintained in Eagle's Minimum Essential Medium (EMEM) with 10% (v/v) fetal bovine serum (HyClone FBS) and 1% (v/v) penicillin-streptomycin at 37°C with 85% humidity and 5% CO₂. Media was refreshed every 2 days. After reaching 80% confluency, the cells were passaged using 0.25% (w/v)trypsin containing ethylenediaminetetraacetic acid (2.2 mM, EDTA·4Na). Experiments were conducted with at least three different passages between 5-12.

3.2. 3D cell encapsulation

Dilute HA-Tz solution was sterile filtered using 0.2 μm Steriflip filter units (EMD Millipore Corporation) prior to lyophilization and maintained under aseptic conditions thereafter. Reconstituted SMR-bisNb (in PBS) and RGD/RGE-TCO (in EMEM) were sterilized using 0.2-μm syringe filters (Pall Corporation, Port Washington, NY). DU145 cells were suspended in a HA-Tz / SMR-bisNb solution at a concentration of 0.5×10⁶ cells/mL. Cell-laden hydrogels (300 μL each) were prepared in 12-mm cell culture inserts as described above and incubated for 1 h at 37°C before the addition of the EMEM media (300 and 700 μL inside and outside the insert, respectively). Seven days later, interfacial ligation of RGD/RGE peptides was carried out on the cellular construct following the procedure mentioned above. Cultures were maintained until day 21, and media was refreshed every other day. The cell-gel constructs were imaged using an Eclipse Ti-E microscope (Nikon, Tokyo, Japan) to obtain bright field images. For immunostaining, hydrogels (50 μL each) were prepared in 48-well glass bottom plates MatTek Corporation, (Ashland, MA) following the same protocol.

3.3. Cell viability and spheroid size

Constructs were stained using the LIVE/DEAD™ viability assay kit (ThermoFisher Scientific) supplemented with a membrane permeable nuclear stain, Hoechst 33342. Specifically, samples were incubated with calcein AM (1:1000 dilution), ethidium homodimer (EthD-1, 1:2000 dilution) and Hoechst 33342 (1:500 dilution) in warm PBS at 37°C for 20 min. After thorough washes with PBS (3 times), samples were inspected under a Zeiss LSM 880 confocal microscope (Carl Zeiss, Oberkochen, Germany). Images were acquired (>10 images per construct) from random sections of the hydrogel, as 150-µm z-stacks with z-axis step size of 7.0 µm and quantified from maximum intensity projections. Cell viability and spheroid size and size distribution were analyzed using ImageJ (National Institutes of Health, Bethesda, MD). After counting EthD-1+ / Hoechst+ cells (dead cells) and Hoechst+ cells (all cells), viability was calculated as the difference between the two over the total cell count. Spheroids were defined as organized cell

clusters with greater than 5 cells. Spheroid size distribution was created using a histogram plot with a 5 µm bin for diameters. The resulting histogram was fitted using Gaussian distribution using OriginPro Software (Northampton, MA).

3.4. Gene expression

Hydrogel constructs were washed thoroughly with PBS, snap frozen on a dry ice / isopropanol mixture, and stored at -80 °C till further use. RNA extraction was performed following our reported methods(*37*) using Trizol (Invitrogen, Carlsbad, CA). One microgram RNA was reverse transcribed using the QuantiTect Reverse Transcription Kit (Qiagen, Hilden, Germany) and the resultant cDNA was diluted 50 folds with nuclease free water. Real time quantitative polymerase chain reaction (qPCR) was performed by combining cDNA templates, primers (400 nM) and Power SYBR green master mix using an ABI 7300 real time PCR system. The relative expression levels of selected genes were monitored. Beta actin (β-actin) was used as endogenous reference gene. The fold change was calculated using 2-ΔΔCT method using a total of three biological repeats for each experimental condition. Primer pairs (Table S1) were purchased from Integrated DNA Technologies (Coralville, IA) and were validated for the DU145 cell line.

3.5. Immunofluorescence

Cell populated hydrogel constructs were washed with PBS three times and fixed with 4% (w/v) paraformaldehyde (PFA, Sigma Aldrich) in PBS for 30 min. For Ki-67 and cleaved caspase-3 staining, constructs were incubated in 0.2% (w/v) Triton X-100 in PBS for 2 h at room temperature, followed by 16-h incubation in 3% (w/v) bovine serum albumin (BSA) in PBS at 4°C. To stain E-cadherin and CD44, samples were permeabilized for 5 min with 0.2% (w/v) Triton X-100 in PBS, followed by blocking with BSA for 2 h at 4 °C. For integrin α₅, samples were permeabilized for 5 min with 0.1% (w/v) Triton X-100 in PBS, followed by overnight blocking with

BSA at 4°C. For vimentin and cortactin, permeabilization was done for 1 h with 0.2% Triton X-100 in PBS at room temperature, with overnight blocking at 4°C. Samples were then treated with primary antibodies with appropriate dilution in 3% BSA (Table S2) overnight at 4°C for E-cadherin, Ki67, CD44, integrin α₅ and cortactin or for 2 h at room temperature for vimentin, and cleaved caspase-3. The primary antibody solution was aspirated, and samples were washed three times using PBS with 0.05% tween 20 (PBST, Sigma Aldrich), with 15-min incubation for each step. Secondary antibodies, Alexa Fluor™ 488 goat anti-mouse or anti-rabbit IgG, along with Alexa FluorTM 568 phalloidin (Life Technologies, Carlsbad, CA), diluted at 1/200 in 3% BSA, were added and samples were incubated for 2 h at room temperature. The solution was aspirated, and the sample was washed with PBST three times. Finally, nuclei were counter stained by 4',6diamidino-2-phenylindole (DAPI, Life Technologies, Carlsbad, CA), diluted at 1/1000 in PBS, was for 20 min at room temperature. For hydrogel constructs in which only nuclei and F-actin were stained, no blocking step was performed. After 1-h permeabilization at room temperature, samples were stained with Alexa Fluor[™] 568 phalloidin, followed by DAPI, as described above. Fluorescent microscopy was performed using Zeiss LSM 880 using Fast Airy scan mode with either C-Apochromat 10×/0.45W or LD LCI Plan-Apochromat 25×/0.8 Imm Korr water objectives. Images were captured as 40 µm z-stacks with 1.0 µm z-axis step size, each 16-bit with sequential frame capture mode. The brightness of each channel was uniformly adjusted for each of the representative images using ZEN 3.0 SR software.

3.6. Image Analyses

Using the region of interest (ROI) manager and the magic wand tool in ImageJ, cells or spheroids were manually traced for F-actin channel. Background correction was applied and using ROI manager, and the cross-sectional area and circularity for RGD-H, RGD-L and RGD-0 were generated separately for at least 20 random maximum intensity projection images and normalized to RGD-0 controls. Fold change in invasion area was defined as invasion index and

was normalized to RGD-0 cultures. Circularity was calculated as $4\pi \times (\text{area/perimeter}^2)$ using ROI manager, with 1.0 being a perfect sphere and lower values for an elongated object(38). A minimum of 20 maximum intensity projection images from three biological replicates were selected for the above analysis. Quantitative observation of morphology and size distribution was made from at least 10 confocal images acquired as maximum intensity projections.

To quantify the total fluorescent intensity for E-cadherin, vimentin and cortactin, ImageJ and the associated plugins were used. Following ethical guidelines (39-41), uniform brightness was applied to captured confocal images using ZEN 3.0 SR software. Image channels were split, and the background intensity was subtracted from the channel for protein of interest. Using Macros plugin with an interactive interpreter, uniform areas were selected for day 7 and 21 images. Total intensity of protein of interest was determined by generating histogram of z-stack and calculating the total count of voxels for the 3D image. Percentage increase or decrease in intensity was calculated by subtracting the final value from the initial value, normalizing the result the initial value, and multiplying by 100.

4. Statistical Analyses

In all experiments, replicates were collected across multiple cell passages on different days, with each passage contributing to at least three replicates as indicated. Sample sizes were chosen based on preliminary experiments to ensure statistical power. For comparison between two groups, unpaired two-tailed Student's t-test with p<0.05 was considered significant. For comparison between multiple groups, one-way or two-way ANOVA followed by Dunnett's test was used, with p<0.05 as significant. Statistical analyses were made using GraphPad Prism (San Diego, CA) version 9.2.0 or JMP Pro 15 (SAS Institute Inc., Cary, NC) and plotted using GraphPad Prism (San Diego, CA) version 9.2.0 and OriginPro 2021b software (Northampton, MA.) Error bars represent standard error of the mean value, unless otherwise stated in the figure caption.

RESULTS

1. Tetrazine ligation with slow/fast dienophiles permits dynamic tuning of gel properties.

The initial HA-based hydrogel was produced via an inverse electron-demand Diels-Alder reaction between tetrazine and norbornene (Fig. 1A). This reaction is biocompatible and bioorthogonal and occurs readily under physiological conditions. With a second order rate constant (k_2) of 10⁻²-10⁰ M⁻¹s⁻¹ (31), it is ideally suited for 3D cell encapsulation via bulk mixing of cell suspension with the crosslinker solution (Fig. 1B). HA-Tz with a 22% tetrazine incorporation (Fig. S1-S2) was used as the macromer and a bifunctional SMR peptide with norbornene linked to the peptide through lysine amines, as a mixture of exo/endo isomers (Fig. S3-S8), was used as the crosslinker. To establish matrices with an optimal stiffness for 3D growth of DU145 cells(42), and to permit time-delayed modifications of the synthetic ECM via tetrazine-TCO ligation (Fig. 1B), hydrogels were prepared at a Tz/Nb molar ratio of 2/1. Characterization by oscillatory rheometry showed that gelation occurred approximately 10 ± 2 min after mixing (Fig. 2A, insert), as evidenced by the crossover of the storage modulus (G') and loss modulus (G"). The G' value continued to increase, reaching a plateau value in 335 ± 16 min. The hydrogels exhibited an average G' and G" value of 300 ± 27 and 1.1 ± 0.1 Pa (Fig. 2A). The storage modulus remained unchanged at frequencies of 0.1 to 10 Hz, indicating the establishment of a stable covalent network (Fig. 2B). The sol fraction and swelling ratio of the hydrogel were characterized as 12.7 \pm 2.7% and 14.0 \pm 1.1, respectively.

To foster cell mobility in the covalent network, a synthetic peptide SMR-bisNb with an MMP cleavage site between the serine (S) and methionine (M) residue (43, 44) was selected as the crosslinker. In the presence of 100 U/mL collagenase type II(45, 46) or type IV(47), hydrogels were degraded in eight days (Fig. 2C). Due to water penetration in the loosened network(48, 49), an initial increase in wet mass was observed within the first two days. Thereafter, the wet weight progressively decreased as more peptide cleavage by collagenase led to solubilization of gel

fragments. No significant weight loss was detected for gels incubated in the enzyme free HBSS buffer.

The cellular constructs developed above contain residue, unreacted tetrazine groups that can be used as reactive handles for user-directed matrix modifications during cell culture. To mimic the dynamic changes occurring in the tumor associated ECM during metastasis, the RGD peptide, derived from type III10 repeat of fibronectin(50), was conjugated to the cellular construct on day 7 using RGD-TCO via a diffusion controlled tetrazine-TCO interfacial ligation (Fig. 1). This is feasible because the cycloaddition reaction between tetrazine and TCO features fast kinetics, high yielding, and high selectivity at low concentrations. With k_2 exceeding 10^6 M-1s-1(28, 33, 51), it is the fastest bioorthogonal reaction reported to date. As shown in Fig. 2D, the interfacial reaction was initiated after the TCO reservoir was loaded on top of the pre-formed hydrogel. The parent, unmodified matrix contained a maximum of 2.5 mM free tetrazine groups. As the TCO molecule diffused into the gel, it instantaneously reacted with the residual tetrazine group at the gel-liquid interface, forming a cycloadduct with dangling RGD. This diffusion-controlled reaction was monitored by the gradual disappearance of the tetrazine chromophore (pink). After 10 h, the remaining free tetrazine groups were completely consumed.

Supplementation of Cy5-TCO in the RGD-TCO reservoir enabled assessment of the spatial distribution of RGD via confocal microscope(52). As shown in Fig. 2E, Cy5 signals were homogenously distributed throughout the hydrogel. Analyses of unconjugated peptide in the wash buffer equilibrated with the hydrogel(53) by UV-Vis spectrometry indicated 96% ± 3% and 94% ± 4% retention in the hydrogels for RGD-TCO and RGE-TCO, respectively (Fig. S21, Fig. 2F). Rheological characterization demonstrated that gels treated with blank PBS and PBS solution of RGD- or RGE-TCO exhibited similar mechanical properties (Fig. 2G-J). In subsequent studies, RGE-TCO was used as a control in place of RGD-TCO(54). Mutating the aspartic acid residue to the glutamic acid negated the ability of the peptide to bind integrins(55, 56) without altering the molecular diffusion and reactivity.

2. RGD-free HA hydrogels promote clonal expansion of PCa cells

Cellular constructs were prepared by dispersing DU145 cells homogeneously in HA-Tz and SMR-bisNb. On day 7, EMEM media was supplemented with RGD-/RGE-TCO to initiate interfacial RGD tagging. On day 8, the TCO media was replaced by the EMEM media and cultures were maintained until day 21. Three TCO reservoirs containing varying amounts of RGD-/RGE-TCO were used to generate modified constructs with high (RGD-H) and low RGD (RGD-L) densities as well as the RGD-free controls (RGD-0) (Fig. 3A).

During the initial 7 days of culture in non-adhesive HA gels, DU145 cells evolved from dispersed single cells on day 1 to compact, multicellular spheroids by day 7 (Fig. 3B). Spheroids were detectable as early as day 3. Cells in individual spheroids were closely packed, with cortical F-actin delineating the cell-cell boundary and the spheroid-ECM interface (Fig. 3C). The size of the spheroids increased over time, and by day 6, spheroid size ranged from 20 to 50 µm (Fig. 3D). Although single cells were evenly distributed in the hydrogel on day 1, by day 7, the size of spheroids in randomly selected areas was heterogenous. This could be due to the heterogenous growth pattern of cancer cells(25).

Cells in the single cell and the spheroid states exhibited distinctly different gene expression patterns (Fig. 3E, F). Our qPCR results show that mRNA levels of epithelial cell marker *CDH1* (E-cadherin) were remarkably higher (29.0 \pm 0.8, p <0.001) and mesenchymal marker *VIM1* (vimentin) was significantly lower (0.5 \pm 0.1, p<0.05) on day 7 compared to day 1. Expression of *CCND1* (cyclin D1), an important regulator of cell cycle progression, was significantly upregulated (6.5 \pm 0.3, p<0.01) on day 7. Overexpression of cyclin D1 has been shown to compromise the activity of cyclin-dependent kinases, leading to neoplastic growth(57). *CD44* (cluster of differentiation 44), a receptor for hyaluronic acid, and *MT1-MMP* (membrane type-1 matrix metalloproteinase), a multifunctional protease that is implicated in cancer progression and ECM degradation, were also significantly upregulated (*CD44*: 7.0 \pm 0.2, p<0.01;

MT1-MMP: 40.0 ± 0.7 , p<0.001) on day 7 as compared to day 1. Higher expression of CD44 has been linked to prostate cancer progression(26, 58). Immunofluorescent characterization of day 7 spheroids confirmed positive staining for CD44 (Fig. 3G). Overall, DU145 cells readily assembled into organized 3D spheroids by day 7 in the MMP-degradable HA hydrogels without any integrin binding peptides.

3. RGD tagging induces spheroid decompaction and cellular outgrowth

Next, interfacial bioorthogonal conjugation was employed to increase the matrix adhesiveness via RGD tagging (Fig. 4A). Seven days after RGD tagging (day 14), isolated tumoroids in RGD-H gels started to de-compact and cellular protrusions were developed along the border of the aggregates. By day 21, almost all multicellular structures developed in RGD-H gels had lost the original compact spherical morphology and became irregularly shaped loose aggregates (Fig. 4B). We observed distinct F-actin rich cellular processes protruding from individual cell clusters (Fig. 4C). Some cells had completely detached from the cluster and dispersed in the matrix as single, spindle-shape cells, while others migrated into and integrated with neighboring structures (Fig. 4B, red arrow heads). In doing so, the heterogenous nature of the cell population was further amplified. At a lower RGD density, the RGD-L cultures contained intact spheroids as well as those with cellular protrusions radiating from the periphery. No merging structures were seen. By contrast, cells remained as compact spheroids in RGD-0 gels without any signs of invasion until day 21 (Fig. 4B, C).

Additional experiments were conducted to evaluate the responses of other prostate cancer cell lines, including PC3, an aggressive bone metastasized prostatic adenocarcinoma cell line, and LNCaP, a less aggressive cell line from lymph node metastasis. By day 18 (Fig. S22) multicellular structures in PC3/RGD-H cultures were abundant, irregularly shaped and some exhibited distinctive cellular protrusions around the border. Contrarily, structures found in PC3/RGD-0 were small and spherical. On the other hand, LNCaP cells remained as multicellular

spheroids irrespective of the culture condition (Fig. S23). Both PC3 and LNCaP cultures maintained high cell viability (Fig. S22, S23) under RGD-0 and RGD-H conditions.

F-actin and nuclei-stained confocal images were used to quantify spheroid size, invasion index, percentage of intact spheroids and circularity. Five days after interfacial tagging (day 12 of culture), DU145 cells remained as spheroids under both RGD-0 and RGD-H conditions (Fig. 5A). On average, spheroids grown in RGD-H hydrogel were larger than those developed in RGD-0 gels, as shown in the spheroid distribution histogram. By day 12, most spheroids grown in RGD-H cultures were in the range 30-65 μ m, and maximum spheroids were around 45 μ m (Fig. 5B). In RGD-0 cultures, most spheroids ranged from 20-50 μ m in diameter, with maximum spheroids around 35 μ m (Fig. 5C). Increasing RGD density led to a progressive and significant increase in invasion index, with the RGD-L and RGD-H cultures being 4.5 \pm 0.8 and 10.7 \pm 1.5 folds higher than the RGD-0 controls, respectively (Fig. 5D). Similarly, the circularity of the multicellular structures and the percentage of spheroids remaining decreased with increasing RGD concentrations (Fig. 5E, F). As the matrix became more adhesive, spheroid size and shape became more heterogeneous (Fig. S24).

Because RGD is known to bind various integrins, including $\alpha_5\beta_1$, $\alpha_8\beta_1$, $\alpha_V\beta_1$, $\alpha_V\beta_3$, $\alpha_V\beta_5$, $\alpha_V\beta_6$, $\alpha_V\beta_8$, $\alpha_{IIb}\beta_3(50)$, qPCR experiments were performed to analyze the expression of various integrins at the transcript level. Our results (Fig. 5G-I, Fig. S25) show that, compared to the day 7 level prior to interfacial ligation, RGD modification at high and low concentrations led to upregulation of the expression of *ITGA5*, *ITGB2*, *ITGB6* and *ITGB8* by day 14, which is 7 days post RGD tagging. Additionally, *ITGAV*, *ITGB1* and *ITGB5* were upregulated in RGD-H cultures. Except for the expression of *ITGB3*, prolonging the culture in a RGD free environment did not significantly alter the expression of other integrins. Finally, the expressions of *ITGA1*, *ITGA2*, *ITGA3*, *ITGA4*, and *ITGA6* remained unaltered. Immunofluorescent characterization revealed that day 10 and day 21 spheroids were stained brightly for integrin α_5 , with localized signals at cell membrane (Fig 5J). However, prior to RGD tagging on day 7, spheroids were stained negatively

for integrin α_5 (Fig S26). Overall, DU145 cells grown in HA gels respond to RGD modification in a concentration dependent manner and the most profound effect was detected at the targeted concentration of 2.5 mM.

We further queried whether interfacial RGD tagging affects cell viability, proliferation, and apoptosis. To this end, constructs were stained with calcein AM (live cells) and Ethdr-1 (dead cells), as well as Hoechst, a cell permeable nuclei dye, and unbiased viability quantification was conducted. One day after cell encapsulation, approximately $78.0 \pm 1.6\%$ and $80.0 \pm 1.5\%$ cells respectively were viable for RGD-H and RGD-0, respectively. At this point, RGD-H and RGD-0 constructs were essentially the same. Cell viability remained unchanged after RGD/RGE tagging on day 7 and throughout the 21 days of culture, irrespective of culture conditions (RGD-H vs RGD-0, Fig. 6A, B). Collectively, these results confirmed the cytocompatibility of the 3D culture platform and that the RGD signal is not a pre-requisite for maintaining cell viability.

Cells grown in RGD-H gels were further stained for Ki67, a nuclear proliferation marker, and active cleaved caspase-3, a crucial mediator of apoptosis. On day 7, overall Ki67 positive cells significantly increased as compared to day 1. For larger spheroids, these cells were primarily located at the periphery of the structures, but for smaller spheroids, proliferative cells were also seen in the center of the structure (Fig. 6C, D, Fig. S27). By day 21, approximately 30.0 ± 2.4% of cells in RGD-H cultures were Ki67+, representing a significant reduction (p < 0.05) from both the day 1 and day 7 levels. At this stage, Ki67 signals were observed in the center of spheroids with less protrusive structures, and very few Ki67+ nuclei were detected in cell clusters with highly protrusive structures. In RGD-0 cultures, many Ki67+ nuclei were detected on day 21 (Fig. S27 B-C). On day 21, 57 ± 3.9% cells in RGD-0 cultures were Ki67+, representing approximately 21% increase (p<0.05) compared to the corresponding RGD-H cultures (Fig. S27C). These results indicate that RGD tagging promoted cell migration at the expense of proliferation. In addition, positive cleaved caspase-3 cells were not detected in day 7 or day 21 spheroids (Fig. 6E), suggesting the absence of apoptosis at the core of spheroids throughout the culture period. To

confirm the sensitivity of our immunostaining protocol, cultures were treated with staurosporine, known to induce apoptosis through both caspase-dependent and caspase-independent mechanisms(59). Under these conditions, cleaved caspase 3 was detected both in 2D and day 7 3D cultures (Fig. S28). Collectively, interfacial RGD tagging led to ECM-mediated cell dissemination at the expense of continued cell proliferation.

4. RGD tagging induced epithelial to mesenchymal transition

To better understand how matrix adhesiveness regulates cell phenotype, cultures were assessed for expression of EMT related markers by qPCR. First, we analyzed the gene expression of RGD-0 cultures on day 21 as compared to that on day 7 (Fig. 7A-D). While *CDH1* expression was increased significantly by 3.00 ± 0.03 folds, the expressions of *VIM1*, *SNA1*, and *SNA2* were significantly reduced by 0.80 ± 0.02 , 0.70 ± 0.03 and 0.80 ± 0.05 folds, respectively. The expressions of *CDH3*, *FN1*, *TWIST1* and *ZEB1* were not changed. These results indicate that prolonged culture of PCa cells in an RGD free environment does not induce EMT.

Next, the gene expression of the RGD-H culture was normalized to the RGD-0 level at day 21 (Fig. 7E-I). Introduction of RGD signals significantly down-regulated *CDH1* expression by 0.70 ± 0.02 fold for RGD-H cultures, but significantly upregulated *CDH3* (an indicator of enhanced cell motility)(60) expression by 1.8 ± 0.1 folds for RGD-H. Meanwhile, *VIM1*, mesenchymal marker and intermediate filament vimentin, was significantly upregulated (2.5 ± 0.2 folds) in RGD-H cultures. Fibronectin (*FN1*) was downregulated (0.8 ± 0.1 folds) in RGD presenting gels and EMT master transcription factors, *SNA1* (Snail1), *SNA2* (Snail2/Slug), *TWIST1* and *ZEB1*, were significantly upregulated upon RGD conjugation. A similar trend in gene expression was observed for day 14 when compared to day 7 spheroids (Fig. S29). Interestingly, the expression of *MMP9*, *MT1-MMP* and *TIMP1* was upregulated in RGD presenting hydrogel while the expression of *SDC1* (syndecan) and *MMP1* remained unaltered (Fig. 7H-I).

The expression of EMT markers were further confirmed by immunofluorescence. On 2D surface, DU145 cells showed bright immunofluorescence for E-cadherin, indicating substantial native expression (Fig. S30). Prior to RGD tagging on day 7, the spheroids exhibited bright staining for E-cadherin at the cell-cell junctions (Fig. 8A). Positive vimentin staining was only found at the periphery of the spheroids where cells were in contact with the synthetic matrix (Fig. 8C). Fourteen days post RGD conjugation (day 21), E-cadherin staining became very diffuse, punctate, and intracellular. Compared to day 7 spheroids, E-cadherin expression reduced by approximately 81% on day 21 (Fig. 8B). On the other hand, vimentin was stained extremely brightly in almost all invading spheroids, as filamentous structures concentrated in regions with distinct cell protrusions. From day 7 to day 21, there was an approximate 54% increase in vimentin expression (Fig. 8D), indicative of the attainment of a mesenchymal phenotype upon RGD tagging. We further stained the intact and invading structures for cortactin, a classical marker for invadopodia, an invasive protrusion exhibiting proteolytic activity uniquely found in aggressive cancer cells(61, 62). Intact spheroids showed diffuse cytoplasmic expression of cortactin while invading tumoroids exhibited distinct cortactin signals in the protrusive structures interacting with the matrix (Fig. 8E), with an estimated 37% increase in cortactin fluorescence intensity from day 7 to day 21 (Fig. 8F). Together these data indicate that HA-based hydrogel with RGD presentation promotes spheroid invasion with a mesenchymal phenotype and invadopodia like protrusive structures (Fig 9).

DISCUSSION

We have developed a biomimetic hydrogel platform that is enzymatically degradable, and dynamically tunable, allowing *in situ* bioorthogonal incorporation of fibronectin derived cell adhesive RGD peptide, which reflects fibronectin overexpression during tumor growth and metastasis(23, 63). Gel stiffness, maintained constant before and after RGD tagging, was matched to that for brain tissues(42) to recreate the metastatic niche. The highly efficient tetrazine

ligation with TCO ensures quantitative, close to 100% conjugation. The exceptional rate also ensured that cells in the gel were not exposed to the soluble ligand, which would otherwise competitively bind integrins(32).

Our results show that dispersed DU145 cells formed compact spheroids with close cellcell contacts after 7 days of culture in the initial RGD-free, MMP-degradable matrix. The ability of DU145 cells to bind HA via CD44 and RHAMM and to remodel the matrix through various secreted enzymes, including HAases and MMPs, facilitates the growth of dispersed single cells into multicellular spheroids in hydrogels lacking integrin binding ligands (27, 58, 64). Increased expression of MT1-MMP could be a response to the SMR crosslinker that is known to be degraded by MMP1, MMP2, MMP3, MMP7, MMP9 and MMP14 (MT1-MMP)(43). Compared to the single cells, cells in the spheroids expressed a higher level of epithelial cell marker, CDH1. Thus, under the initial culture conditions, DU145 cells remained epithelial cell-like with strong cell-cell contacts, forming compact spheroids due to the proximity of clonally expanded daughter cells in the covalent network. Upregulation of CCND1, a regulator of cell cycle and a biomarker of cancer phenotype(65), has been shown to compromise cyclin dependent kinases activity, leading to neoplastic growth(57). The primary tumoroids also expressed a high level of CD44, indicative of an invasive, stem cell-like phenotype. CD44 positive cancer stem cells are known to mediate tumor initiation and metastasis(66). Analysis of immortalized prostate cancer cell lines (LNCaP and DU145) revealed that CD44 positive cells exhibited more invasive properties in Matrigel, whereas CD44 negative were non-invasive (66). In colorectal cancer, even a single CD44 positive cell can produce a tumoroid exhibiting stem cell-like properties in vitro and generate a xenograft tumor similar to the primary tumor, indicating the functional importance of cancer stem cells for cancer initiation and progression(67). Collectively, the initial RGD-free network facilitated the establishment of the primary tumoroids with metastatic potential.

To induce cell invasion, we introduced fibronectin derived RGD signals to the ECM surrounding the day-7 tumoroids. As one of the most abundant glycoproteins in the native ECM,

fibronectin plays important roles in cell adhesion, growth, differentiation, and migration through integrin mediated signaling. RGD interacts with integrins to activate several tyrosine kinases and protein kinase signal transduction pathways. It is possible that more RGD in the matrix leads to the development of more traction force, which in turn upregulates integrin expression(68). In various types of cancers, reprogramming of tumor stroma is accompanied by upregulation of fibronectin and their receptors(63, 69). For example, upregulation of several ECM proteins, including fibronectin and laminin, was found to correlate with poor patient outcome in pancreatic ductal carcinoma. Analysis via immunohistochemistry revealed that high levels of relevant integrins were detected and fibronectin mediated adhesions via $\alpha_V \beta_1$ and $\alpha_2 \beta_1$ integrins occurred *in vivo*. Additionally, splicing of the *FN1* gene in adults occurs in cancer and FN1 modifications contribute to ECM biosynthesis, alterations, or degradations, thereby modulating tumor ECM composition and promoting metastasis(69-71). Hence, we reasoned that it is necessary to introduce this cell adhesion cue to the ECM in a time-delayed manner to recapitulate the dynamic changes in tumor microenvironment and to reconstitute ECM-receptor interactions.

Upon RGD tagging, tumoroids grew bigger and by day 21, spheroids in RGD-H gels developed F-actin rich protrusive structures and started to invade into the surrounding ECM. Contrarily, tumoroids developed under RGD-0 conditions remained intact and spherical. We further showed that cell dissemination from the tumoroids and invasion into the matrix were dependent on RGD density. Since tetrazine-TCO reaction is highly efficient and proceeds with close to 100% yield, the RGD density in the modified ECM was readily varied by stoichiometric mixing of RGD-/RGE-TCO in the diffusing media. As RGD density increases, the spheroids became less compact, the invasive protrusions extended further, and the invasion area became larger. In the hydrogel with the maximum RGD density, the cellular protrusions were highly pronounced, neighboring structures were seen coalescing and integrating, and almost no intact spheroids were present. In hydrogels with a low RGD density, some tumoroids remained spherical and others had developed invasive fronts.

RGD tagging on day 7 did not negatively impact the overall cell viability throughout the remaining 14 days of culture. RGD tagging led to an immediate increase in the size of the spheroids, followed by decompaction and invasion. In RGD-0 gels, spheroids stayed compact, although moderate increase in spheroid size over time was observed, the size was smaller than those found in RGD-H before significant invasion was observed. Interestingly, staining of the proliferation marker Ki67 revealed that an overall lower percentage of cells were Ki67 positive in RGD-H cultures at day 21 as compared to day 1, day 7 and day 21 RGD-0. DU145 cells proliferated rapidly during the initial 7 days of culture through close cell-cell interactions. As the matrix was rendered more adhesive, the number of proliferative cells at the periphery of the cell clusters decreased, although a few Ki67 positive cells were seen at the core of spheroids on day 21. Under these conditions, apoptotic cells were not detected. Instead of stimulating cell proliferation, RGD immobilization led to the strengthening of cell-matrix adhesion and reorganization of F-actin cytoskeleton to promote the development of invasive cellular protrusions. In other words, time-delayed presentation of the RGD signal transformed the inherently less invasive DU145 cells (18) into a more aggressive phenotype.

We do not expect to observe the same cellular responses to interfacial RGD tagging given the wide spectrum of phenotype, polarization, EMT status, ECM stiffness and cell-cell/cell-ECM interactions across different PCa cell lines. Owing to these differences, cells adapt differently to our 3D culture platform. Interestingly, the order of cell dissemination (DU145 > PC3 > LNCaP) observed here correlated with their metastatic potential. In agreement with our observations, primary and non-transformed cells when cultured in Matrigel, formed compact spheroids, whereas more aggressive prostate cancer cell lines formed poorly differentiated spheroids or aggressively invading structures(18).

To understand how ECM composition regulates cell function and phenotype, we measured the expression of genes encoding EMT markers. RGD conjugation led to a significant upregulation of the expression of mesenchymal markers, including vimentin (VIM1), P-cadherin

(CDH3), and EMT master regulators Snail (SNAI1), Slug (SNAI2), TWIST and ZEB1. Interestingly, prolonged culture of DU145 cells in RGD-free gels beyond day 7 led to a marked increase in CDH1 (E-cadherin) expression, while mesenchymal markers and EMT transcription factors were downregulated when compared to the levels on day 7. Compared to RGD-0 cultures, cells in RGD tagged hydrogels expressed significantly higher levels of MMP9 and MT1-MMP. A similar trend was observed at the protein level, with marked increase in expression of vimentin and decreased expression of E-cadherin post RGD conjugation. F-actin polymerization in a bundled state along with breakdown of adherens junctions can translocate E-cadherin from cell surface to cytoplasm and drive localized cellular protrusions, all indicative of directed cell migration and EMT(11, 12). These data indicate that RGD tagging induced cell dissemination from the spheroids and invasion into the ECM, as evidenced by loss of cadherin-mediated cell-cell adhesion within the spheroid, increase in cell-ECM attachment, and proteolytic breakdown of basement membrane, all characteristics of EMT.

Abundant expression of E-cadherin and minimal expression of vimentin are required to form compact spheroids. During cancer progression, loss of cell polarity and intercellular contacts are accompanied with the attainment of cell motility and the invasion of the basement membrane. Loss of E-cadherin expression through transcriptional repression by Snail/Slug or Twist contributes to the adaptation of invasive behaviors. The upregulation of certain integrins and surface expression of integrin α_5 after RGD tagging further enhanced cell-matrix adhesion, promoting cell survival and phenotypic switches (60, 72, 73). Although DU145 spheroids exhibited complete loss of cell-cell contacts after RGD conjugation, only a small subset of cancer cells might be in state of complete EMT or intermediate states of partial EMT. These cells exhibit inherent phenotypic plasticity and become the leading cells to establish tumor at a secondary site(74-77). Moreover, EMT and dissemination of individual cancer cells have been linked to loss of E-cadherin and increased integrin mediated ECM adhesions. Additionally, intracellular binding partners of $\alpha_5\beta_1$ integrins can promote metastasis by sensitizing cancer cells to changes in the

surrounding matrix. This interdependency of integrins-cadherin is an important regulator of plasticity of cancer invasion *in vivo*(78).

Recent studies have shown that cortactin, a cytoskeletal protein and SRC kinase substrate that is highly expressed in high grade metastatic cancers, plays an important role in promoting cell motility and its presence in actin-rich invadopodia structures is associated with ECM degradation by tumor cells(79). As a master regulator of branched actin assembly, cortactin localizes to sites of dynamic actin assembly through the Arp2/3 and F-actin binding sites (80-84). Live cell imaging has shown that cortactin recruitment precedes a few minutes before the proteases like MT1-MMP, MMP2 and MMP9 trafficking to sites of ECM degradation(85, 86). Positive cortactin staining of protrusive structures developed in RGD-H constructs further substantiates the development of invasive phenotype.

Collectively, employing modular building blocks and bioorthogonal reactions, we have successfully constructed a reductionist 3D culture platform that is reproducible, flexible, and tunable, allowing straightforward interrogation of the effects of a particular ECM cue on the morphology, migration, and phenotype of prostate cancer cells. The bioorthogonal hydrogel platform provides a cell permissive and cell instructive microenvironment that fosters the initial cell-cell and later cell-matrix interactions to enable the establishment of a metastasis-mimetic tumor model. Using this platform, we demonstrated EMT-like behavior of DU145 cells for the first time. The engineered model is valid as it replicates a well-known phenomenon in cancer biology, i.e., the increase in matrix adhesiveness due to excessive fibronectin deposition during tumorigenesis and metastasis (63,69). While we cannot completely recapitulate the complex metastatic niche, our platform has the potential to increase predictive value of pre-clinical drug research. Incorporation of stromal cells and nerve or vascular components in the existing construct will likely produce a more physiologically relevant model.

CONCLUSION

In summary, we present an innovative hydrogel platform that supports the growth, assembly, and migration of DU145 cells in 3D. The modular design of the hydrogel allows time-delayed, user-directed presentation of cell adhesive peptide motifs at variable densities without altering the biomechanical properties of the hydrogel. The tunable platform enabled systematic investigations of the roles of ECM signals in cancer cell proliferation and invasion. The initial RGD free, MMP degradable matrix supported the clonal expansion of dispersed single cells to form multicellular spheroids with close cell-cell contacts. RGD tagging led to a downregulation of the expression of epithelial markers, and an upregulation of the expression of mesenchymal markers and master EMT transcription factors. RGD conjugation induced spheroid decompaction with loss of E-cadherin, and promoted the formation of protrusive, vimentin and cortactin positive 'invadopodia'-like structures. The mesenchymal characteristics and the migratory behaviors observed in our hydrogel-based model are reminiscent of the early stage of cancer progression The engineered model presented here can be used for testing and screening innovative anticancer therapies targeting metastasis.

ACKNOWLEDGEMENT

This work was supported in part by NIH (NIDCR: R01 DE029655, NIDCD: R01 DC014461 and NIGMS: R01 GM132460) and NSF (DMR 1809612, DMR 2011824). Instrumentation and core facility support was made possible by NIH (S10 OD016361, P20 GM103446, P20 GM139760) and NSF (CHE-0840401, CHE-1229234, IIA-1301765) grants. The authors also acknowledge the use of facilities and instrumentation supported by NSF through the University of Delaware Materials Research Science and Engineering Center (DMR 2011824). We thank Drs. Jeff Caplan, Sylvain le Marchand and Chandran Sabanayagam for their guidance on confocal imaging. We thank Genzyme-Sanofi for providing HA.

DATA AVAILABILITY

As part of an ongoing study, the raw/processed data required to reproduce these findings are available from the corresponding author on reasonable request.

REFERENCES:

- 1. R. L. Siegel, K. D. Miller, A. Jemal, Cancer statistics, 2019. *CA Cancer J Clin* **69**, 7-34 (2019).
- 2. P. Rawla, Epidemiology of prostate cancer. World J Oncol 10, 63-89 (2019).
- J. Cuzick, M. A. Thorat, G. Andriole, O. W. Brawley, P. H. Brown, Z. Culig, R. A. Eeles, L. G. Ford, F. C. Hamdy, L. Holmberg, D. Ilic, T. J. Key, C. La Vecchia, H. Lilja, M. Marberger, F. L. Meyskens, L. M. Minasian, C. Parker, H. L. Parnes, S. Perner, H. Rittenhouse, J. Schalken, H. P. Schmid, B. J. Schmitz-Dräger, F. H. Schröder, A. Stenzl, B. Tombal, T. J. Wilt, A. Wolk, Prevention and early detection of prostate cancer. *Lancet Oncol* 15, e484-492 (2014).
- P. Harnden, M. D. Shelley, H. Clements, B. Coles, R. S. Tyndale-Biscoe, B. Naylor, M. D. Mason, The prognostic significance of perineural invasion in prostatic cancer biopsies: a systematic review. *Cancer* 109, 13-24 (2007).
- 5. F. Z. Chen, X. K. Zhao, Prostate cancer: current treatment and prevention strategies. *Iran Red Crescent Med J* **15**, 279-284 (2013).
- 6. R. Baghban, L. Roshangar, R. Jahanban-Esfahlan, K. Seidi, A. Ebrahimi-Kalan, M. Jaymand, S. Kolahian, T. Javaheri, P. Zare, Tumor microenvironment complexity and therapeutic implications at a glance. *Cell Commun Signal* **18**, 59 (2020).
- 7. P. Beri, B. F. Matte, L. Fattet, D. Kim, J. Yang, A. J. Engler, Biomaterials to model and measure epithelial cancers. *Nat Rev Mater* **3**, 418-430 (2018).
- 8. E. Cukierman, R. Pankov, D. R. Stevens, K. M. Yamada, Taking cell-matrix adhesions to the third dimension. *Science* **294**, 1708-1712 (2001).

- 9. I. Chatzistefanou, J. Lubek, K. Markou, R. A. Ord, The role of perineural invasion in treatment decisions for oral cancer patients: A review of the literature. *J Craniomaxillofac Surg* **45**, 821-825 (2017).
- 10. R. B. Nagle, A. E. Cress, Metastasis update: human prostate carcinoma invasion via tubulogenesis. *Prostate Cancer* **2011**, 249290 (2011).
- 11. M. Yilmaz, G. Christofori, EMT, the cytoskeleton, and cancer cell invasion. *Cancer Metastasis Rev* **28**, 15-33 (2009).
- 12. S. E. Leggett, A. M. Hruska, M. Guo, I. Y. Wong, The epithelial-mesenchymal transition and the cytoskeleton in bioengineered systems. *Cell Commun Signal* **19**, 32 (2021).
- 13. M. W. Tibbitt, K. S. Anseth, Hydrogels as extracellular matrix mimics for 3D cell culture. *Biotechnol Bioeng* **103**, 655-663 (2009).
- 14. K. Wolf, P. Friedl, Molecular mechanisms of cancer cell invasion and plasticity. *Br J Dermatol* **154 Suppl 1**, 11-15 (2006).
- 15. K. M. Yamada, M. Sixt, Mechanisms of 3D cell migration. *Nat Rev Mol Cell Biol* **20**, 738-752 (2019).
- B. Galateanu, A. Hudita, E. I. Biru, H. Iovu, C. Zaharia, E. Simsensohn, M. Costache, R.
 C. Petca, V. Jinga, Applications of polymers for organ-on-chip technology in urology.
 Polymers (Basel) 14, 1668 (2022).
- 17. G. Greenburg, E. D. Hay, Epithelia suspended in collagen gels can lose polarity and express characteristics of migrating mesenchymal cells. *J Cell Biol* **95**, 333-339 (1982).
- 18. V. Härmä, J. Virtanen, R. Mäkelä, A. Happonen, J. P. Mpindi, M. Knuuttila, P. Kohonen, J. Lötjönen, O. Kallioniemi, M. Nees, A comprehensive panel of three-dimensional models for studies of prostate cancer growth, invasion and drug responses. *PLoS One* 5, e10431 (2010).
- 19. A. Dongre, R. A. Weinberg, New insights into the mechanisms of epithelial-mesenchymal transition and implications for cancer. *Nat Rev Mol Cell Biol* **20**, 69-84 (2019).

- 20. M. Zeisberg, E. G. Neilson, Biomarkers for epithelial-mesenchymal transitions. *J Clin Invest* **119**, 1429-1437 (2009).
- 21. M. J. Bissell, D. Radisky, Putting tumours in context. *Nat Rev Cancer* 1, 46-54 (2001).
- M. Zoetemelk, M. Rausch, D. J. Colin, O. Dormond, P. Nowak-Sliwinska, Short-term 3D culture systems of various complexity for treatment optimization of colorectal carcinoma.
 Sci Rep 9, 7103 (2019).
- C. R. Below, J. Kelly, A. Brown, J. D. Humphries, C. Hutton, J. Xu, B. Y. Lee, C. Cintas, X. Zhang, V. Hernandez-Gordillo, L. Stockdale, M. A. Goldsworthy, J. Geraghty, L. Foster, D. A. O'Reilly, B. Schedding, J. Askari, J. Burns, N. Hodson, D. L. Smith, C. Lally, G. Ashton, D. Knight, A. Mironov, A. Banyard, J. A. Eble, J. P. Morton, M. J. Humphries, L. G. Griffith, C. Jørgensen, A microenvironment-inspired synthetic three-dimensional model for pancreatic ductal adenocarcinoma organoids. *Nat Mater* 21, 110-119 (2022).
- 24. L. A. Gurski, A. K. Jha, C. Zhang, X. Jia, M. C. Farach-Carson, Hyaluronic acid-based hydrogels as 3D matrices for in vitro evaluation of chemotherapeutic drugs using poorly adherent prostate cancer cells. *Biomaterials* **30**, 6076-6085 (2009).
- Y. Hao, A. B. Zerdoum, A. J. Stuffer, A. K. Rajasekaran, X. Jia, Biomimetic Hydrogels Incorporating Polymeric Cell-Adhesive Peptide To Promote the 3D Assembly of Tumoroids. *Biomacromolecules* 17, 3750-3760 (2016).
- 26. X. Xu, A. K. Jha, D. A. Harrington, M. C. Farach-Carson, X. Jia, Hyaluronic acid-based hydrogels: from a natural polysaccharide to complex networks. *Soft Matter* **8**, 3280-3294 (2012).
- 27. L. A. Gurski, X. Xu, L. N. Labrada, N. T. Nguyen, L. Xiao, K. L. van Golen, X. Jia, M. C. Farach-Carson, Hyaluronan (HA) interacting proteins RHAMM and hyaluronidase impact prostate cancer cell behavior and invadopodia formation in 3D HA-based hydrogels. *PLoS One* 7, e50075 (2012).

- M. L. Blackman, M. Royzen, J. M. Fox, Tetrazine ligation: fast bioconjugation based on inverse-electron-demand Diels-Alder reactivity. *J Am Chem Soc* 130, 13518-13519 (2008).
- 29. R. M. Desai, S. T. Koshy, S. A. Hilderbrand, D. J. Mooney, N. S. Joshi, Versatile click alginate hydrogels crosslinked via tetrazine-norbornene chemistry. *Biomaterials* **50**, 30-37 (2015).
- F. Jivan, R. Yegappan, H. Pearce, J. K. Carrow, M. McShane, A. K. Gaharwar, D. L. Alge,
 Sequential thiol-ene and tetrazine click reactions for the polymerization and
 functionalization of hydrogel microparticles. *Biomacromolecules* 17, 3516-3523 (2016).
- 31. S. Eising, A. H. J. Engwerda, X. Riedijk, F. M. Bickelhaupt, K. M. Bonger, Highly stable and selective tetrazines for the coordination-assisted bioorthogonal ligation with vinylboronic Aaids. *Bioconjugate Chemistry* **29**, 3054-3059 (2018).
- 32. Y. Hao, J. Song, A. Ravikrishnan, K. T. Dicker, E. W. Fowler, A. B. Zerdoum, Y. Li, H. Zhang, A. K. Rajasekaran, J. M. Fox, X. Jia, Rapid bioorthogonal chemistry enables in situ modulation of the stem cell behavior in 3D without external triggers. ACS Appl Mater Interfaces 10, 26016-26027 (2018).
- 33. M. T. Taylor, M. L. Blackman, O. Dmitrenko, J. M. Fox, Design and synthesis of highly reactive dienophiles for the tetrazine-trans-cyclooctene ligation. *J Am Chem Soc* **133**, 9646-9649 (2011).
- 34. K. T. Dicker, J. Song, A. C. Moore, H. Zhang, Y. Li, D. L. Burris, X. Jia, J. M. Fox, Coreshell patterning of synthetic hydrogels via interfacial bioorthogonal chemistry for spatial control of stem cell behavior. *Chem Sci* **9**, 5394-5404 (2018).
- 35. M. Royzen, G. P. Yap, J. M. Fox, A photochemical synthesis of functionalized transcyclooctenes driven by metal complexation. *J Am Chem Soc* **130**, 3760-3761 (2008).
- 36. H. Zhang, W. S. Trout, S. Liu, G. A. Andrade, D. A. Hudson, S. L. Scinto, K. T. Dicker, Y. Li, N. Lazouski, J. Rosenthal, C. Thorpe, X. Jia, J. M. Fox, Rapid bioorthogonal chemistry

- turn-on through enzymatic or long wavelength photocatalytic activation of tetrazine ligation. *J Am Chem Soc* **138**, 5978-5983 (2016).
- 37. A. B. Zerdoum, E. W. Fowler, X. Jia, Induction of fibrogenic phenotype in human mesenchymal stem cells by connective tissue growth factor in a hydrogel model of soft connective tissue. *ACS Biomater Sci Eng* **5**, 4531-4541 (2019).
- 38. H. J. An, H. S. Kim, J. A. Kwon, J. Song, I. Choi, Adjustable and versatile 3D tumor spheroid culture platform with interfacial elastomeric wells. *ACS Appl Mater Interfaces* **12**, 6924-6932 (2020).
- 39. J. Jonkman, C. M. Brown, G. D. Wright, K. I. Anderson, A. J. North, Tutorial: guidance for quantitative confocal microscopy. *Nat Protoc* **15**, 1585-1611 (2020).
- 40. D. W. Cromey, Avoiding twisted pixels: ethical guidelines for the appropriate use and manipulation of scientific digital images. *Sci Eng Ethics* **16**, 639-667 (2010).
- 41. M. H. Shihan, S. G. Novo, S. J. Le Marchand, Y. Wang, M. K. Duncan, A simple method for quantitating confocal fluorescent images. *Biochem Biophys Rep* **25**, 100916 (2021).
- 42. Z. Liu, L. Wang, H. Xu, Q. Du, L. Li, E. S. Zhang, G. Chen, Y. Wang, Heterogeneous responses to mechanical force of prostate cancer cells inducing different metastasis patterns. *Adv Sci (Weinh)* **7**, 1903583 (2020).
- 43. J. Patterson, J. A. Hubbell, Enhanced proteolytic degradation of molecularly engineered PEG hydrogels in response to MMP-1 and MMP-2. *Biomaterials* **31**, 7836-7845 (2010).
- 44. B. E. Turk, L. L. Huang, E. T. Piro, L. C. Cantley, Determination of protease cleavage site motifs using mixture-based oriented peptide libraries. *Nat Biotechnol* **19**, 661-667 (2001).
- 45. J. L. Holloway, H. Ma, R. Rai, J. A. Burdick, Modulating hydrogel crosslink density and degradation to control bone morphogenetic protein delivery and in vivo bone formation. *J Control Release* **191**, 63-70 (2014).

- C. B. Rodell, R. J. Wade, B. P. Purcell, N. N. Dusaj, J. A. Burdick, Selective proteolytic degradation of guest-host assembled, injectable hyaluronic acid hydrogels. *ACS Biomater Sci Eng* 1, 277-286 (2015).
- 47. J. A. Beamish, B. A. Juliar, D. S. Cleveland, M. E. Busch, L. Nimmagadda, A. J. Putnam, Deciphering the relative roles of matrix metalloproteinase- and plasmin-mediated matrix degradation during capillary morphogenesis using engineered hydrogels. *J Biomed Mater Res B Appl Biomater* **107**, 2507-2516 (2019).
- 48. S. H. Lee, J. S. Miller, J. J. Moon, J. L. West, Proteolytically degradable hydrogels with a fluorogenic substrate for studies of cellular proteolytic activity and migration. *Biotechnol Prog* 21, 1736-1741 (2005).
- 49. Y. Qiu, J. J. Lim, L. Scott, R. C. Adams, H. T. Bui, J. S. Temenoff, PEG-based hydrogels with tunable degradation characteristics to control delivery of marrow stromal cells for tendon overuse injuries. *Acta Biomater* **7**, 959-966 (2011).
- 50. E. Ruoslahti, RGD and other recognition sequences for integrins. *Annu Rev Cell Dev Biol* **12**, 697-715 (1996).
- 51. J. L. Seitchik, J. C. Peeler, M. T. Taylor, M. L. Blackman, T. W. Rhoads, R. B. Cooley, C. Refakis, J. M. Fox, R. A. Mehl, Genetically encoded tetrazine amino acid directs rapid site-specific in vivo bioorthogonal ligation with trans-cyclooctenes. *J Am Chem Soc* 134, 2898-2901 (2012).
- 52. A. Ravikrishnan, H. Zhang, J. M. Fox, X. Jia, Core-Shell Microfibers via Bioorthogonal Layer-by-Layer Assembly. *ACS Macro Lett* **9**, 1369-1375 (2020).
- 53. L. Zhang, J. Shi, J. Feng, H. Klocker, C. Lee, J. Zhang, Type IV collagenase (matrix metalloproteinase-2 and -9) in prostate cancer. *Prostate Cancer Prostatic Dis* **7**, 327-332 (2004).
- 54. E. Koivunen, D. A. Gay, E. Ruoslahti, Selection of peptides binding to the alpha 5 beta 1 integrin from phage display library. *J Biol Chem* **268**, 20205-20210 (1993).

- 55. S. Takahashi, M. Leiss, M. Moser, T. Ohashi, T. Kitao, D. Heckmann, A. Pfeifer, H. Kessler, J. Takagi, H. P. Erickson, R. Fässler, The RGD motif in fibronectin is essential for development but dispensable for fibril assembly. *J Cell Biol* **178**, 167-178 (2007).
- 56. S. Astrof, R. O. Hynes, Fibronectins in vascular morphogenesis. *Angiogenesis* **12**, 165-175 (2009).
- 57. S. Qie, J. A. Diehl, Cyclin D1, cancer progression, and opportunities in cancer treatment. *J Mol Med (Berl)* **94**, 1313-1326 (2016).
- 58. S. Ekici, W. H. Cerwinka, R. Duncan, P. Gomez, F. Civantos, M. S. Soloway, V. B. Lokeshwar, Comparison of the prognostic potential of hyaluronic acid, hyaluronidase (HYAL-1), CD44v6 and microvessel density for prostate cancer. *Int J Cancer* 112, 121-129 (2004).
- C. A. Belmokhtar, J. Hillion, E. Ségal-Bendirdjian, Staurosporine induces apoptosis through both caspase-dependent and caspase-independent mechanisms. *Oncogene* 20, 3354-3362 (2001).
- 60. W. Yu, L. Yang, T. Li, Y. Zhang, Cadherin signaling in cancer: its functions and role as a therapeutic target. *Front Oncol* **9**, 989 (2019).
- M. A. Magalhaes, D. R. Larson, C. C. Mader, J. J. Bravo-Cordero, H. Gil-Henn, M. Oser,
 X. Chen, A. J. Koleske, J. Condeelis, Cortactin phosphorylation regulates cell invasion
 through a pH-dependent pathway. *J Cell Biol* 195, 903-920 (2011).
- 62. K. Stock, R. Borrink, J. H. Mikesch, A. Hansmeier, J. Rehkämper, M. Trautmann, E. Wardelmann, W. Hartmann, J. Sperveslage, K. Steinestel, Overexpression and Tyr421-phosphorylation of cortactin is induced by three-dimensional spheroid culturing and contributes to migration and invasion of pancreatic ductal adenocarcinoma (PDAC) cells. Cancer Cell Int 19, 77 (2019).
- 63. J. P. Wang, A. Hielscher, Fibronectin: how its aberrant expression in tumors may improve therapeutic targeting. *J Cancer* **8**, 674-682 (2017).

- 64. C. S. Gomez, P. Gomez, J. Knapp, M. Jorda, M. S. Soloway, V. B. Lokeshwar, Hyaluronic acid and HYAL-1 in prostate biopsy specimens: predictors of biochemical recurrence. *J Urol* **182**, 1350-1356 (2009).
- 65. E. A. Musgrove, C. E. Caldon, J. Barraclough, A. Stone, R. L. Sutherland, Cyclin D as a therapeutic target in cancer. *Nat Rev Cancer* **11**, 558-572 (2011).
- 66. G. J. Klarmann, E. M. Hurt, L. A. Mathews, X. Zhang, M. A. Duhagon, T. Mistree, S. B. Thomas, W. L. Farrar, Invasive prostate cancer cells are tumor initiating cells that have a stem cell-like genomic signature. *Clin Exp Metastasis* 26, 433-446 (2009).
- L. Du, H. Wang, L. He, J. Zhang, B. Ni, X. Wang, H. Jin, N. Cahuzac, M. Mehrpour, Y. Lu,
 Q. Chen, CD44 is of functional importance for colorectal cancer stem cells. *Clin Cancer Res* 14, 6751-6760 (2008).
- 68. J. C. Kuo, Mechanotransduction at focal adhesions: integrating cytoskeletal mechanics in migrating cells. *J Cell Mol Med* **17**, 704-712 (2013).
- 69. S. Spada, A. Tocci, F. Di Modugno, P. Nisticò, Fibronectin as a multiregulatory molecule crucial in tumor matrisome: from structural and functional features to clinical practice in oncology. *J Exp Clin Cancer Res* **40**, 102 (2021).
- 70. M. Antia, G. Baneyx, K. E. Kubow, V. Vogel, Fibronectin in aging extracellular matrix fibrils is progressively unfolded by cells and elicits an enhanced rigidity response. *Faraday Discuss* **139**, 229-249; discussion 309-225, 419-220 (2008).
- 71. C. C. Sprenger, S. R. Plymate, M. J. Reed, Aging-related alterations in the extracellular matrix modulate the microenvironment and influence tumor progression. *Int J Cancer* **127**, 2739-2748 (2010).
- 72. D. A. Stewart, C. R. Cooper, R. A. Sikes, Changes in extracellular matrix (ECM) and ECM-associated proteins in the metastatic progression of prostate cancer. *Reprod Biol Endocrinol* **2**, 2 (2004).

- 73. O. Leshem, S. Madar, I. Kogan-Sakin, I. Kamer, I. Goldstein, R. Brosh, Y. Cohen, J. Jacob-Hirsch, M. Ehrlich, S. Ben-Sasson, N. Goldfinger, R. Loewenthal, E. Gazit, V. Rotter, R. Berger, TMPRSS2/ERG promotes epithelial to mesenchymal transition through the ZEB1/ZEB2 axis in a prostate cancer model. *PLoS One* **6**, e21650 (2011).
- 74. I. J. Fidler, The pathogenesis of cancer metastasis: the 'seed and soil' hypothesis revisited. *Nat Rev Cancer* **3**, 453-458 (2003).
- 75. H. Hugo, M. L. Ackland, T. Blick, M. G. Lawrence, J. A. Clements, E. D. Williams, E. W. Thompson, Epithelial--mesenchymal and mesenchymal--epithelial transitions in carcinoma progression. *J Cell Physiol* **213**, 374-383 (2007).
- 76. B. Baum, J. Settleman, M. P. Quinlan, Transitions between epithelial and mesenchymal states in development and disease. *Semin Cell Dev Biol* **19**, 294-308 (2008).
- 77. I. J. Fidler, E. Gruys, M. A. Cifone, Z. Barnes, C. Bucana, Demonstration of multiple phenotypic diversity in a murine melanoma of recent origin. *J Natl Cancer Inst* **67**, 947-956 (1981).
- 78. H. Hamidi, J. Ivaska, Every step of the way: integrins in cancer progression and metastasis. *Nat Rev Cancer* **18**, 533-548 (2018).
- 79. M. Yin, W. Ma, L. An, Cortactin in cancer cell migration and invasion. *Oncotarget* **8**, 88232-88243 (2017).
- 80. E. Nieto-Pelegrin, N. Martinez-Quiles, Distinct phosphorylation requirements regulate cortactin activation by TirEPEC and its binding to N-WASP. *Cell Commun Signal* **7**, 11 (2009).
- 81. T. Uruno, J. Liu, P. Zhang, Fan Yx, C. Egile, R. Li, S. C. Mueller, X. Zhan, Activation of Arp2/3 complex-mediated actin polymerization by cortactin. *Nat Cell Biol* **3**, 259-266 (2001).

- 82. N. S. Bryce, E. S. Clark, J. L. Leysath, J. D. Currie, D. J. Webb, A. M. Weaver, Cortactin promotes cell motility by enhancing lamellipodial persistence. *Curr Biol* **15**, 1276-1285 (2005).
- 83. T. Katsube, S. Togashi, N. Hashimoto, T. Ogiu, H. Tsuji, Filamentous actin binding ability of cortactin isoforms is responsible for their cell-cell junctional localization in epithelial cells. *Arch Biochem Biophys* **427**, 79-90 (2004).
- 84. A. M. Weaver, A. V. Karginov, A. W. Kinley, S. A. Weed, Y. Li, J. T. Parsons, J. A. Cooper, Cortactin promotes and stabilizes Arp2/3-induced actin filament network formation. *Curr Biol* **11**, 370-374 (2001).
- 85. V. V. Artym, Y. Zhang, F. Seillier-Moiseiwitsch, K. M. Yamada, S. C. Mueller, Dynamic interactions of cortactin and membrane type 1 matrix metalloproteinase at invadopodia: defining the stages of invadopodia formation and function. *Cancer Res* **66**, 3034-3043 (2006).
- 86. E. T. Bowden, M. Barth, D. Thomas, R. I. Glazer, S. C. Mueller, An invasion-related complex of cortactin, paxillin and PKCmu associates with invadopodia at sites of extracellular matrix degradation. *Oncogene* **18**, 4440-4449 (1999).

FIGURE CAPTION

Figure 1. Bioorthogonal tuning of hydrogel properties to induce EMT. **(A)** Hydrogels were fabricated via slow Tz-Nb cycloaddition reaction using tetrazine modified HA (HA-Tz) and an MMP-degradable crosslinker (SMR-bisNb) at a Tz/Nb molar ratio of 2/1. RGD ligand was covalently conjugated to the synthetic ECM via fast Tz-TCO ligation through a diffusion-controlled mechanism. RGD density was tuned by varying the molar ratio of RGD-TCO and RGE-TCO. **(B)** DU145 cells in MMP-degradable HA gels spontaneously assembled into multicellular spheroids in 3D. Seven days post encapsulation, the RGD signal was introduced. RGD tagging promoted decompaction of spheroids and invasive processes were developed around the spheroids. Figures for hydrogels were created using BioRender.com.

Figure 2. Hydrogel synthesis, modification, and characterization. (A-B) Representative rheological measurements, including time sweep (A) and frequency sweep (B), of bulk gels prepared with HA-Tz and SMR-bisNb. (C) Gravimetric evaluation of hydrogel degradation by collagenase II and IV (100 U/mL). (D) Tetrazine-TCO interfacial ligation enabled in-situ modification of hydrogel with RGD-TCO. The TCO reservoir was loaded on the top of the hydrogel (labeled with dotted line). The TCO molecules diffused into the hydrogel and conjugated to the network through the unreacted Tz groups. The disappearance of pink color reflected the consumption of tetrazine groups and the immobilization of RGD. (E) Representative confocal image of a hydrogel modified with Cy5/RGD-TCO via interfacial tetrazine ligation. Cy5 signal was homogeneously distributed throughout the gel. (F) Quantification of peptide conjugation efficiency by UV-Vis. n=3, Error bars represent SEM, ns: non-significant. (G-J) Representative rheological measurements of hydrogel after 48 h treatment with a blank PBS reservoir (G, H) or a reservoir containing 2.5 mM RGD-TCO (I, J).

Figure 3. Characterization of 3D cultures prior to RGD-tagging. **(A)** Flow chart for 3D cell culture experiments. **(B)** Bright-field images of RGD-0 cultures on day 1 and 7. **(C)** Representative confocal images of fluorescently stained RGD-0 cultures on day 1 and 7. Blue: DAPI, red: F-actin. **(D)** Spheroid size distribution represented as a histogram for day 6 RGD-0 cultures. **(E, F)** Gene expression analyses of RGD-0 cultures on day 7. Expression was normalized to that for day 1 cultures. n=3, Error bar represent SEM, *: p < 0.05, **: p<0.01, ***: p<0.001, β-actin as the reference gene. **(G)** Immunofluorescence characterization of CD44 expression on day-7 RGD-0 cultures.

Figure 4. Effects of interfacial RGD tagging on tumoroid morphology. **(A)** RGD density in the construct was controlled by varying the molar ratio of RGD-TCO and RGE-TCO in the TCO reservoir. **(B)** Bright-field images of RGD-0, RGD-L and RGD-H cultures on day 1, 7, 14 and 21. Red arrowheads point to protrusions around the tumoroids. Scale bar: 50 μm. **(C)** Representative confocal images of day 21 fluorescently stained for DAPI (blue) and F-actin (yellow).

Figures 5. Morphological (A-F, and J) and molecular (G-I) characterizations of hydrogel derived tumoroids. **(A)** Confocal images of day 12 cultures stained for F-actin and nuclei. Scale bar: 100μm, **(B-C)** Spheroid size and size distribution for day 12 cultures for RGD-H (B) and RGD-0 (C). Solid line represents Gaussian fit. **(D-F)** Quantification of day 21 cultures in terms of invasion index (D), circularity (E) and percent intact spheroids (F). **(G-I)** Quantification of integrin expression by qPCR after 14 days of 3D culture as compared to day 7. n=3, Error bars represent SEM, * p < 0.05, ** p<0.01, β-actin as reference gene. **(J)** Immunofluorescence characterization of integrin α5 expression by DU145 cells after 10 and 21 days of culture under RGD-H conditions.

Figure 6. Characterization of RGD-H cultures in terms of cell viability (A, B), proliferation (C, D) and apoptosis (E). **(A)** Confocal images of DU145 cells stained with calcein AM (live cells, green)

and ethidium homodimer-1(dead cells, red) after 1, 7, 14 and 21 days of culture in RGD-0 and RGD-H. White circles highlight dead cells. **(B)** Quantification of percent viable cells based on live/dead staining. **(C)** Quantification of percentage of Ki67 positive nuclei on day 1, 7, and 21 for RGD-H cultures. *: p<0.05, **: p<0.01 **(D, E)** Immunofluorescence characterization of protein expression by DU145 cells grown in RGD-H for 7 and 21 days. Cell proliferation was assessed by Ki67 staining (D) and cell apoptosis was assessed by cleaved caspase 3 staining (E).

Figure 7. Analyses of the expression of EMT markers by qPCR. **(A-D)** EMT marker expression of RGD-0 culture on day 21 as compared to day 7. Data was normalized to the same RGD-0 conditions on day 7. n=3, Error bars represent SEM, *: p < 0.05, **: p<0.01, β-actin as reference gene. **(E-I)** EMT marker expression by RGD-0 and RGD-H cultures on day 21. Data was normalized to the respective RGD-0 conditions on day 21. n=3, Error bars represent SEM, *: p < 0.05, **: p<0.01, β-actin as the reference gene.

Figure 8. Characterization of the expression of E-cadherin (A, B), vimentin (C, D) and cortactin (E, F) by immunofluorescence. DU145 cells were grown in RGD-H gels for 7 and 21 days. E-cadherin was used as the epithelial cell marker, vimentin as mesenchymal marker, and cortactin as invadopodium marker. Quantification was based on the total fluorescent intensity, by generating histogram of z-stack and calculating the total count of voxels for the 3D image. Percentage increase or decrease in intensity was calculated by subtracting the final value from the initial value, normalizing the result the initial value, and multiplying by 100. n=3, Error bars represent SEM, *: p < 0.05, **: p<0.01, ***: p<0.001.

Figure 9: Schematic representation of phenotypic changes observed in RGD-H cultures from day 1 through day 21.

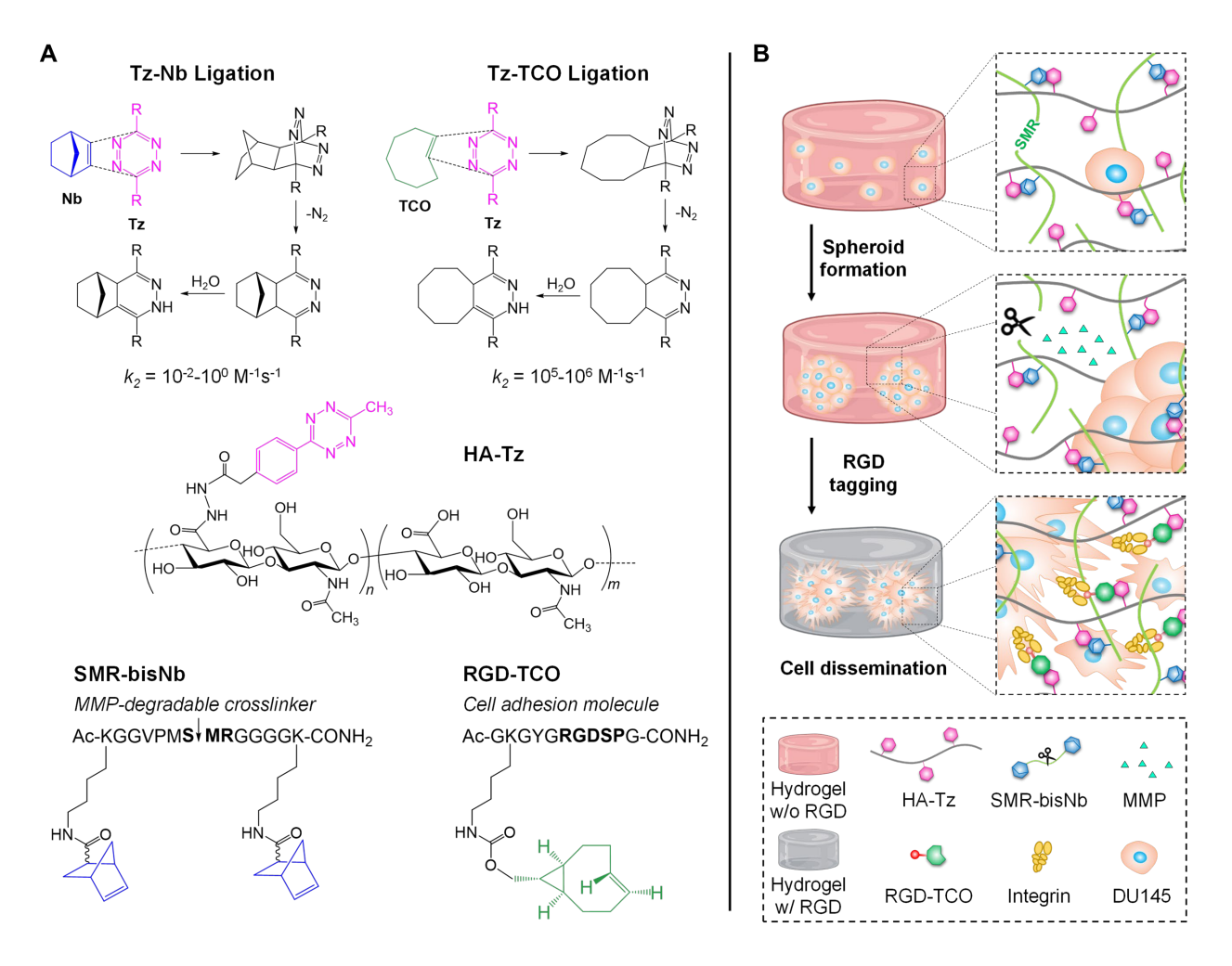


Figure 1.

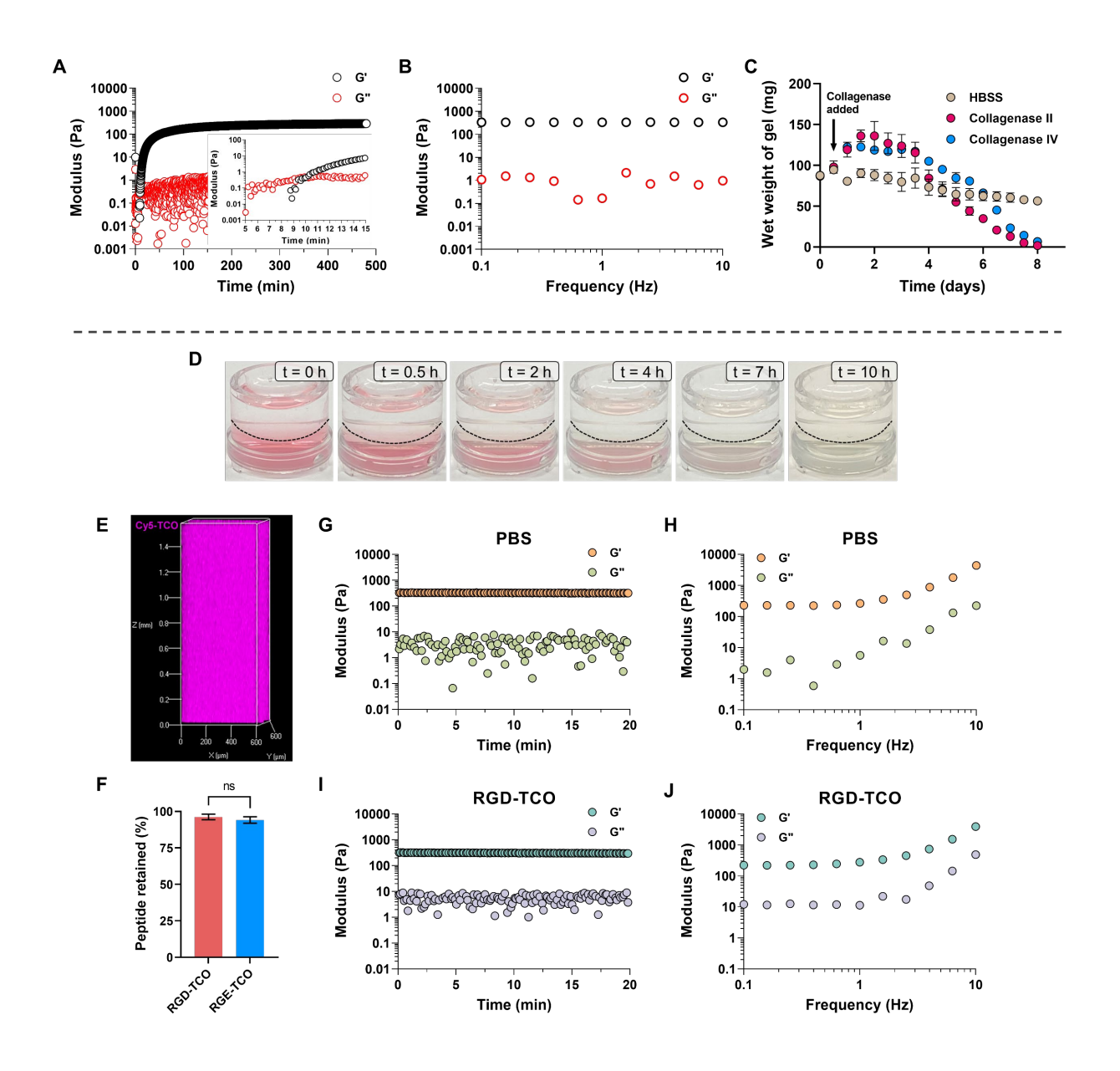


Figure 2.

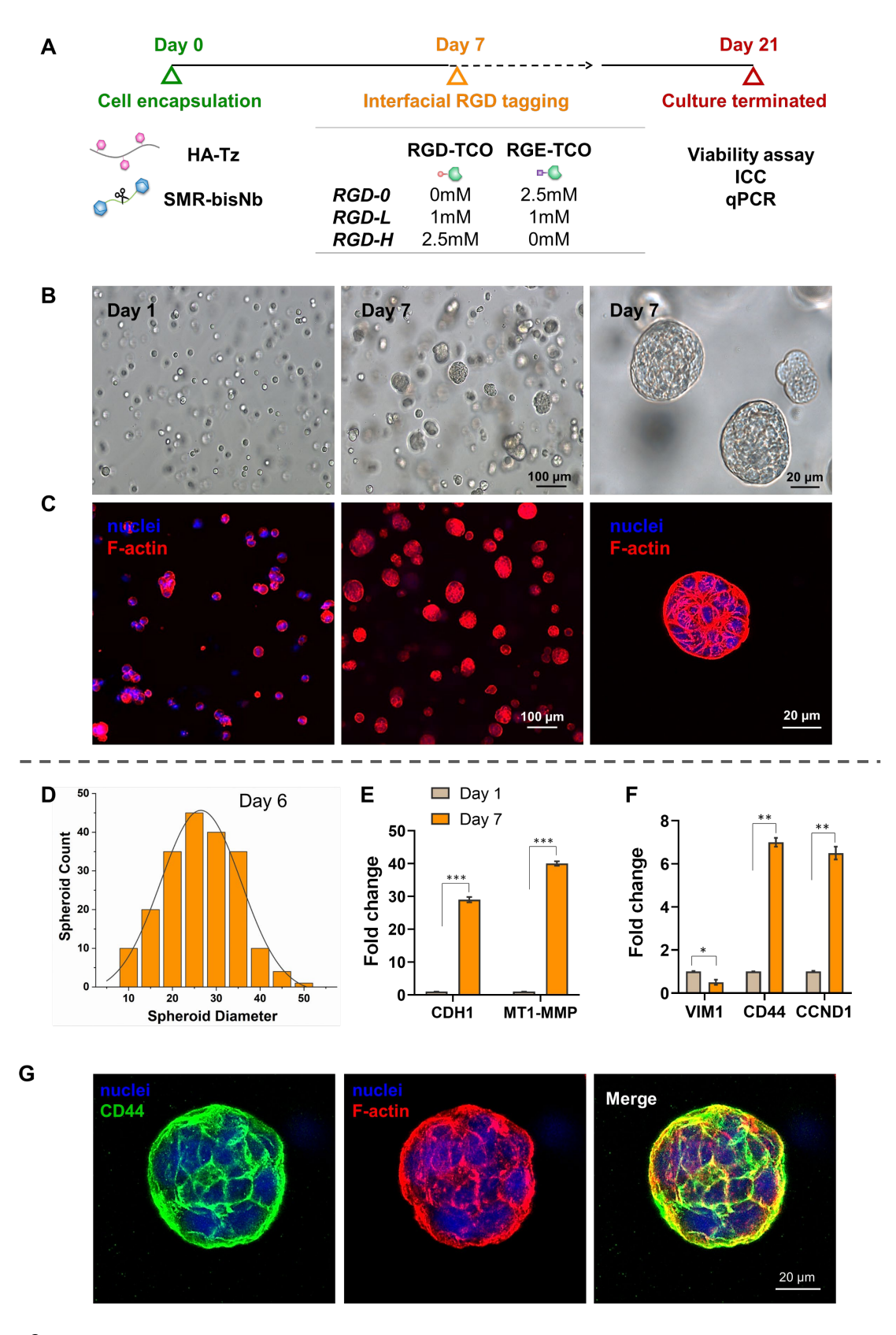


Figure 3.

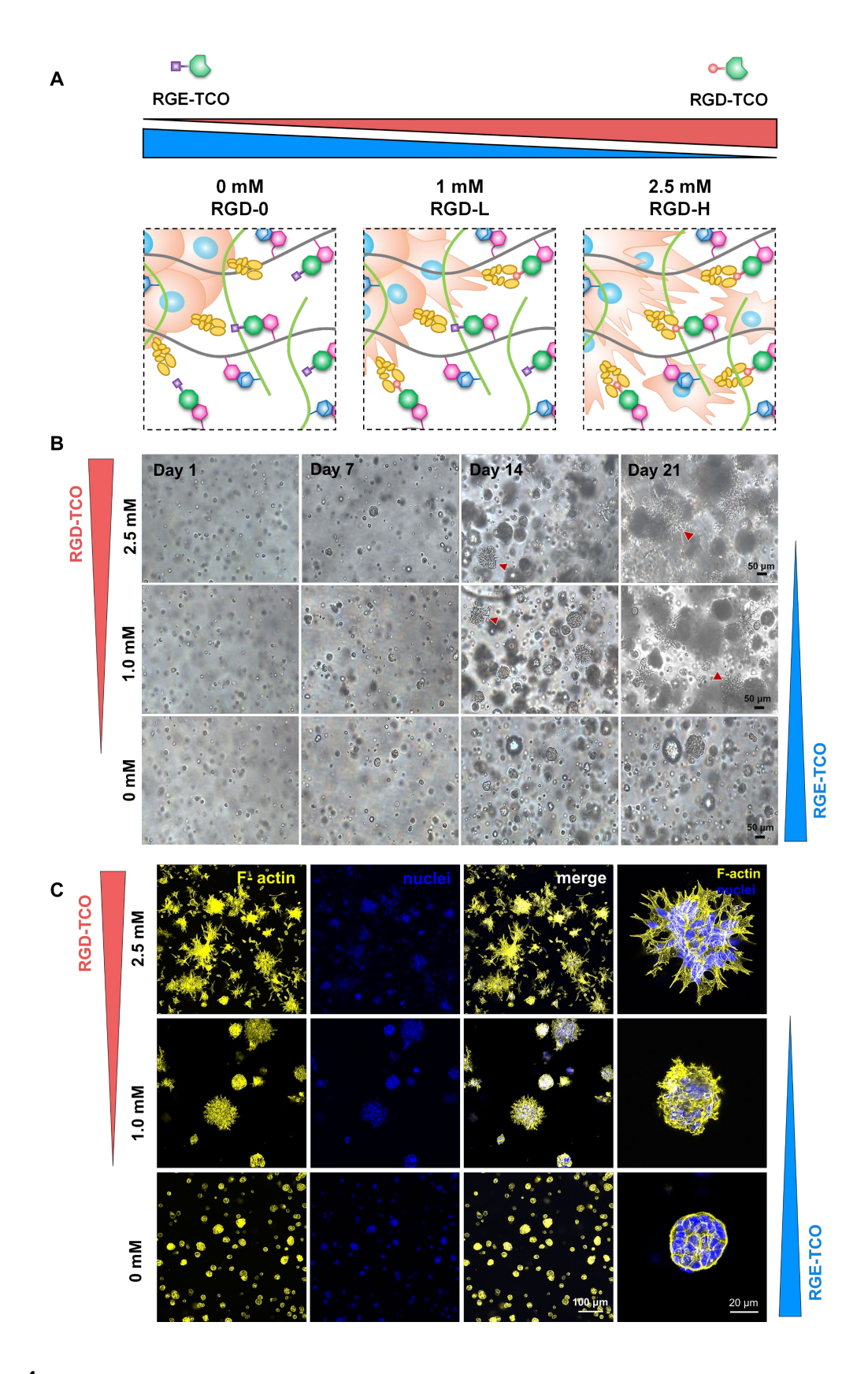


Figure 4.

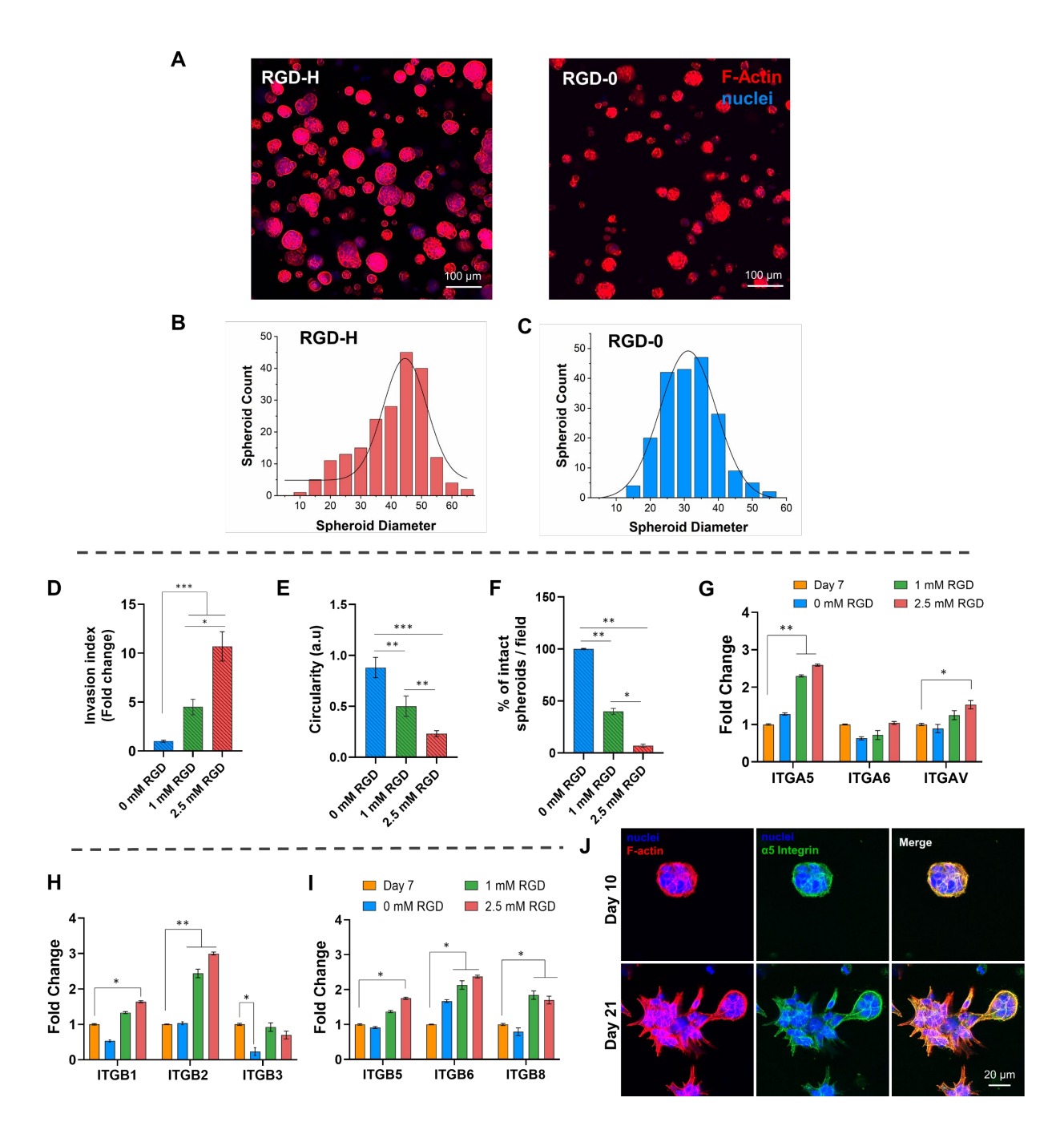


Figure 5.

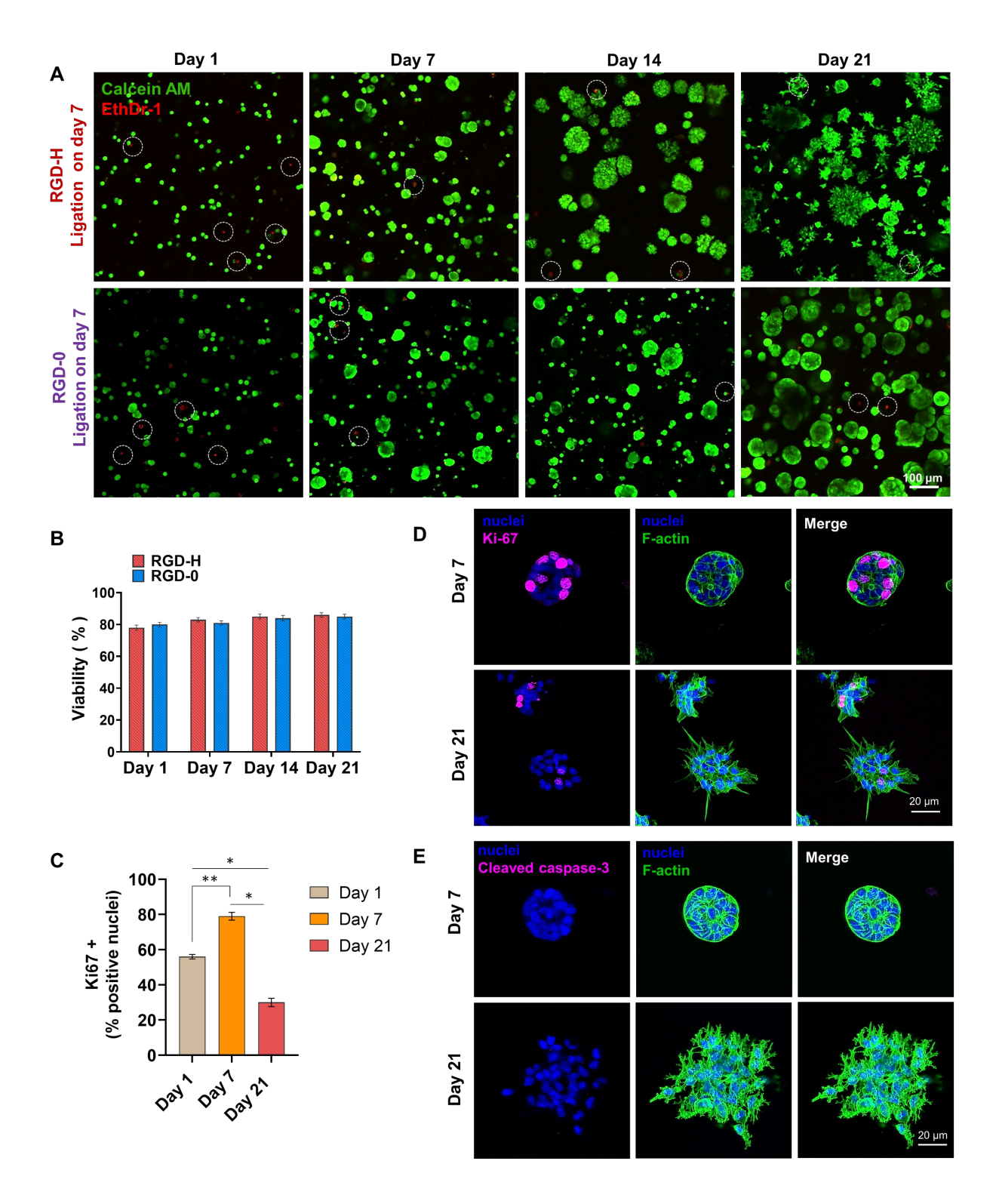


Figure 6.

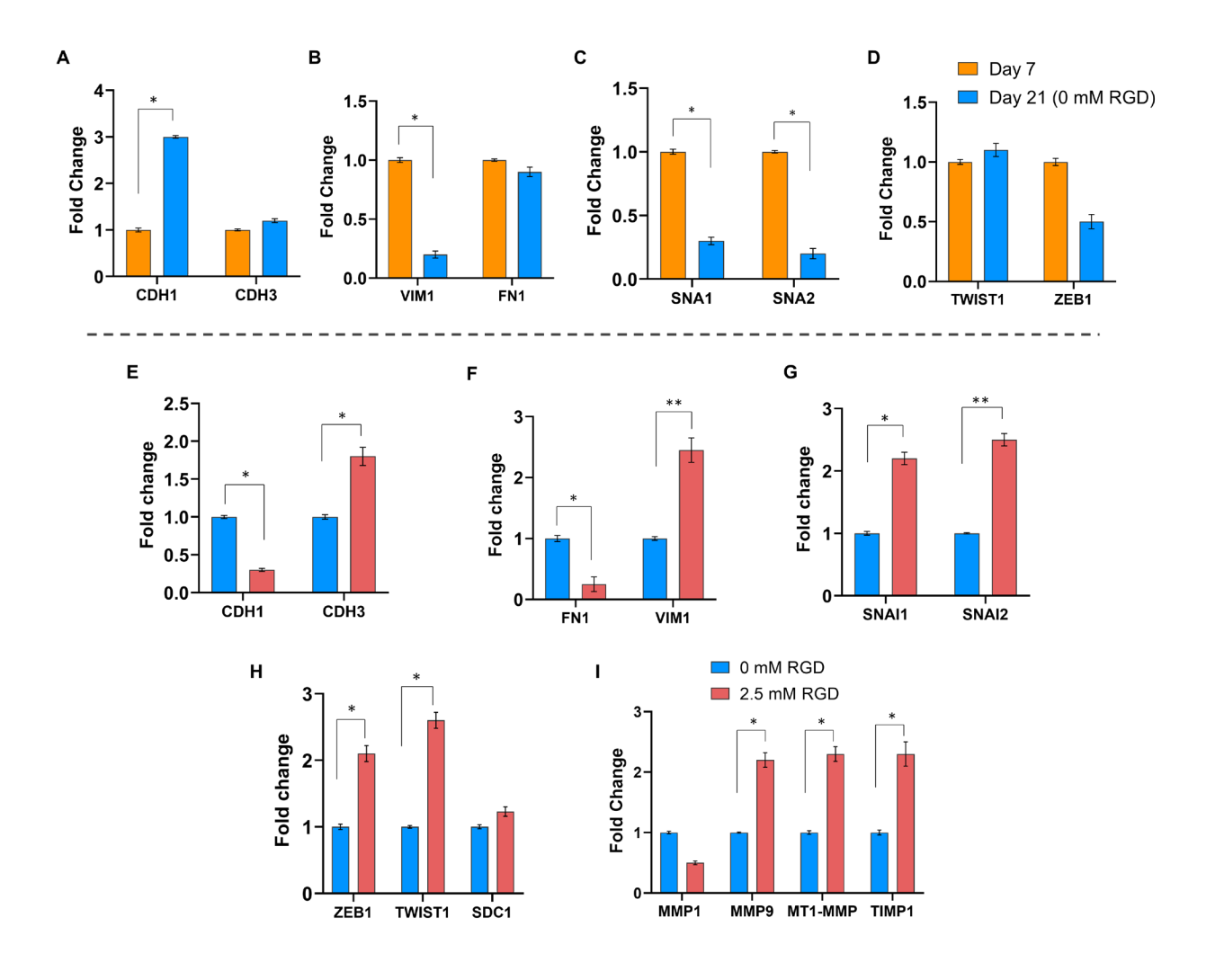


Figure 7.

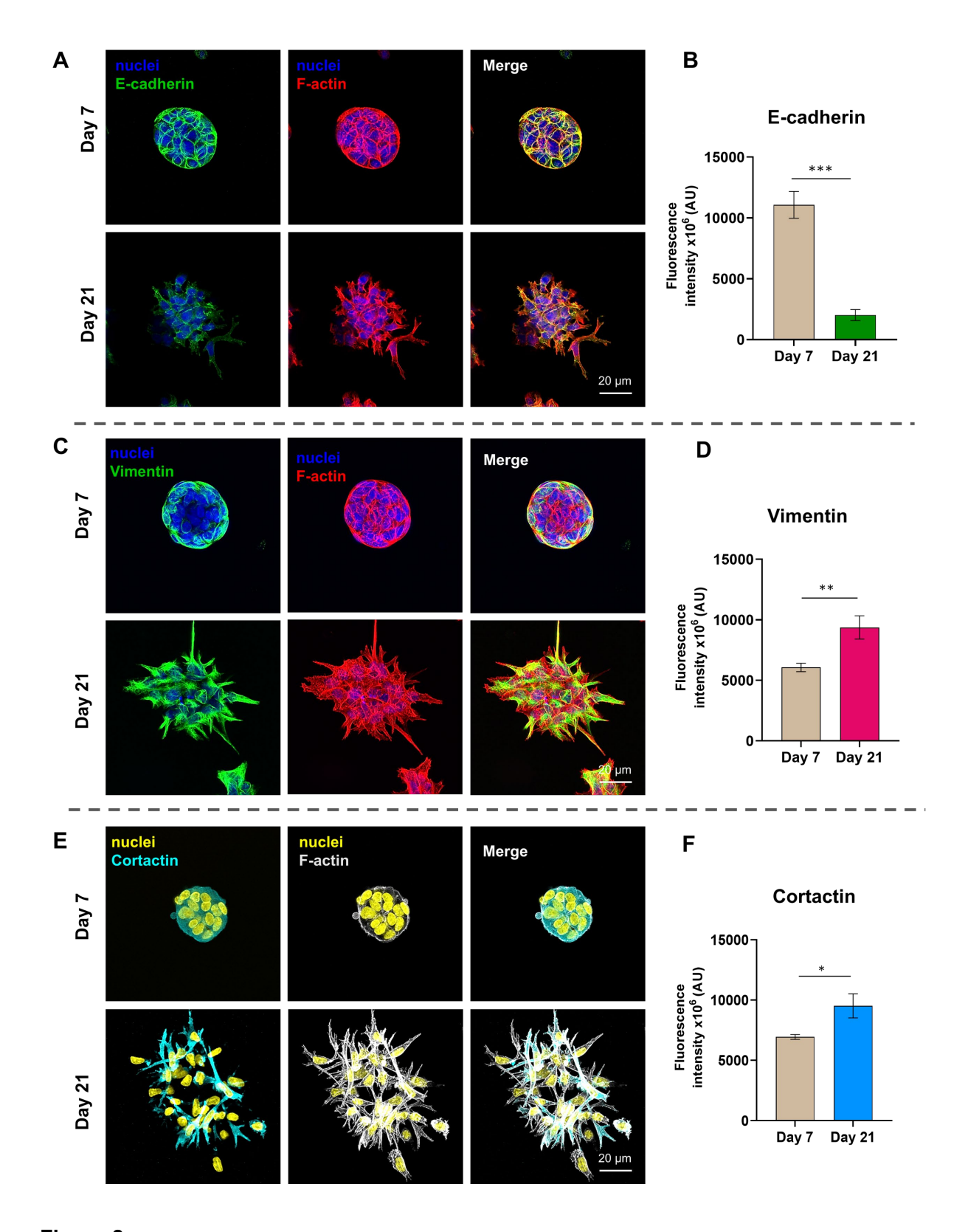


Figure 8.

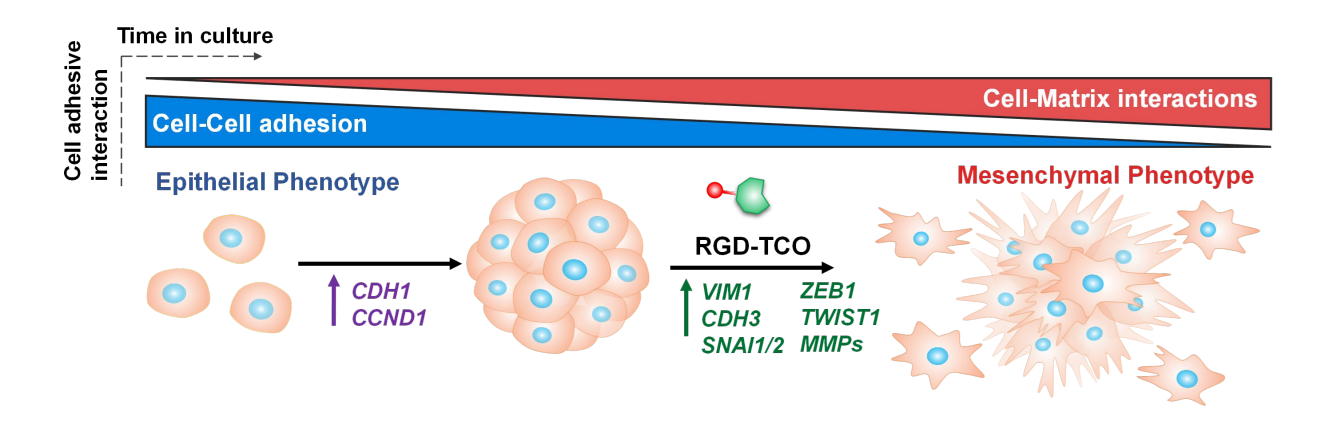


Figure 9.